January 6, 2000
CERN/SPSC 2000-04
SPSC M642

ATOMIC SPECTROSCOPY AND COLLISIONS USING SLOW ANTIPROTONS

Progress report

ASACUSA Collaboration

Azuma, T.[1], Bakos, J. S.[2], Bluhme, H.[3], Charlton, M.[4], Dörner, R.[5], Eades, J.[6], Fujiwara, M.C.[7], Funakoshi, R.[7], Hayano, R.S.[7], Higaki, H.[8], Hoekstra, R.[9], Hori, M.[7], Horváth, D.[2], Hyodo, T.[8], Ichioka, T.[8], Ishikawa, T.[7], Iwasaki, M.[10], Juhász, B.[11], Kambara, T.[12], Ketzer, B.[6], Knudsen, H.[3], Kojima, T.[12], Komaki, K.[8], Kuga, T.[8], Kumakura, M.[13], Kuroda, N.[8], Kuroki, K.[8], McCullough, R.W.[14], Merrison, J.[3], Mikkelsen, U.[3], Møller, S. P.[15], Mohri, A.[12], Morita, N.[13], Nakai, Y.[12], Oshima, N.[12], Rothard, H,[16], Sakaguchi, J.[7], Scheidenberger, C.[17], Schmidt-Böcking, H.[5], Slevin, J.[18], Suzuki, K.[7], Tanuma, H.[19], Thompson, W.R.[3], Torii, H. A.[8], Uggerhøj, E.[15], Ujvári, B.[11], Ullrich, J.[20], Wada, M.[12], Widmann, E.[7], Yamaguchi, H.[7], Yamazaki, T.[21], Yamazaki, Y.[8,12], Yoshiki Franzén, K.[8]

1) Institute of Applied Physics, Tsukuba University, Tenno-dai, Tsukuba 305-8573, Japan
2) KFKI Research Institute for Particle and Nuclear Physics, H–1525 Budapest, Hungary
3) Institute of Physics and Astronomy, University of Aarhus, DK–8000 Aarhus C, Denmark
4) Department of Physics, University of Wales Swansea, Sigleton Park, Swansea SA2 8PP, Wales, UK
5) Institut für Kernphysik, University of Frankfurt, D–60486 Frankfurt, Germany
6) CERN, CH–1211 Geneva 23, Switzerland
7) Department of Physics, University of Tokyo, Hongo, Bunkyo-ku, Tokyo 113 Japan
8) Institute of Physics, University of Tokyo, Komaba, Meguro-ku, Tokyo 153, Japan
9) KVI, Zernikelaan 25, 9747 AA Groningen, The Netherlands
10) Department of Physics, Tokyo Institute of Technology, Meguro-ku, Tokyo 152, Japan
11) Department of Experimental Physics, Lajos Kossuth University, H-4001 Debrecen, Hungary
12) RIKEN, Wako 351-01, Japan
13) Institute for Molecular Science, Okazaki 444, Japan
14) The Queen's University of Belfast, Belfast BT7 1NN, N. Ireland, UK
15) Institute for Storage Ring Facilities, University of Aarhus, DK–8000 Aarhus C, Denmark
16) Ciril -Lab. Mixte CEA-CNRS, Rue Claude Bloch BP5133, 14040 Caen Cedex, France
17) GSI, D–64291 Darmstadt, Germany
18) Department of Experimental Physics, St. Patrick's College, Maynooth, Ireland
19) Department of Physics, Tokyo Metropolitan University, Hachioji 192-03, Japan
20) Universität Freiburg, Hermann-Herder-Str. 3, D–79104 Freiburg, Germany
21) Japan Society for the Promotion of Science, 5-3-1 Kojimachi, Chiyoda-ku, Tokyo 102, Japan

Contents

1 Introduction **1**
- 1.1 Physics goals . . . 1
- 1.2 Phase 1-2-3 Strategy . . . 2
- 1.3 Plans for the Year 2000 . . . 4

2 Status report **5**
- 2.1 Antiprotonic helium phase 1 preparations status . . . 5
  - 2.1.1 AD beam window and beam profile monitor for 100 MeV/c . . . 5
  - 2.1.2 Cryogenic target for high-density measurements with and without microwaves . . . 6
  - 2.1.3 Laser system . . . 8
  - 2.1.4 Microwave system for hyperfine structure measurements . . . 8
  - 2.1.5 Čerenkov counters to detect delayed annihilation of antiprotonic helium . . . 10
- 2.2 Radio frequency quadrupole decelerator construction[1] . . . 10
  - 2.2.1 Supplements to the design report . . . 10
  - 2.2.2 Present status . . . 12
  - 2.2.3 Future plans . . . 13

3 Phase 2 experiments **15**
- 3.1 Measurement of $\overline{p}$ energy loss at very low energies . . . 15
  - 3.1.1 ElectroStatic Analyzer . . . 16
  - 3.1.2 Target . . . 16
  - 3.1.3 Particle detection and diagnostics . . . 17
  - 3.1.4 Measurement Scheme . . . 18
- 3.2 Antiprotonic helium atom studies in low-density helium . . . 19
  - 3.2.1 Preparation status . . . 19
  - 3.2.2 Higher resolution spectroscopy . . . 20
  - 3.2.3 Studies of initial capture processes . . . 24

4 Development of an ultra slow antiproton beam with the electron cooling technique **27**
- 4.1 Scheme of Ultra Slow Antiproton Production . . . 27
- 4.2 Superconducting Solenoid and the ASACUSA Trap . . . 28
- 4.3 Extraction of Antiproton Beam . . . 30

A Appendix – ElectroStatic Analyzer (ESA) design detail[2] **34**
- A.1 ESA electrodes . . . 34
- A.2 Dispersion . . . 34
- A.3 Length of electrodes, radius of curvature . . . 34
- A.4 Gap distance . . . 34
- A.5 Gas cell . . . 35
- A.6 Length of drifts . . . 35
- A.7 Simulations . . . 35
- A.8 Beam steering . . . 37
- A.9 Particle detection and diagnostics . . . 37
- A.10 Estimated count rates, lower limit of energy . . . 37
- A.11 Calibration - cross check . . . 38

1 Introduction

In October 1997 we presented our proposal CERN SPSC/ 97-19, SPSC P-307 to the SPSC committee, in which we outlined our plans for a series of AD experiments on "Atomic Spectroscopy And Collisions Using Slow Antiprotons" (ASACUSA). This proposal follows up some years of similar work at LEAR, and consists of three experimental phases. The first phase was concerned with experiments using the 5.3 MeV AD beam alone , the second with experiments requiring a Radio Frequency Quadrupole Decelerator (RFQD) acting as an AD post-decelerator to reach keV energies, and the third with experiments in which an antiproton trap would be attached to the RFQD to allow experiments with eV antiproton beams. In a letter dated 10 November 1997, we were informed that the SPSC committee had approved the first phase and encouraged construction of the RFQD, but would await development of the latter device before making any recommendations to the Research Board concerning the second and third phases.

In the meantime we have installed and tested all the phase 1 equipment and reproduced one of our LEAR results on antiprotonic helium spectroscopy at the AD. In addition the RFQD has been constructed and awaits tests at Aarhus and CERN during the first half of 2000. Finally the phase 3 trap has been installed and partially tested in Tokyo. In this report we first (Section 2) summarise the present status of the phase 1 installations, present our plans for running phase 1 experiments in 2000, and summarise the status of the RFQ. We then (Section 3) present more details concerning experiments planned for phase 2, and on the existing or planned experimental apparatus for carrying them out. In section 4 we describe the status of the phase 3 trap.

Concerning the phase 2 experiments we ask for the SPSC's conditional approval pending success of the RFQD tests (expected by the summer of 2000).

1.1 Physics goals

The goals of ASACUSA are to study bound or continuum states of antiprotons and simple atoms. Depending on the assumptions made, such studies either test the CPT theorem or the many$(>= 3)$-body theories of such systems. Thus, if we assume the CPT invariance between the properties of the proton and the antiproton, as the theoretical calculations do, the agreement is a signature of the excellence of theoretical treatments and calculation techniques of the Coulombic three-body system including QED corrections. On the other hand, if we take the calculation results for granted, this in turn gives a stringent test of the fundamental constants of the antiproton and therefore tests the CPT theorem. Fig. 1 illustrates the relationship between these two approaches.

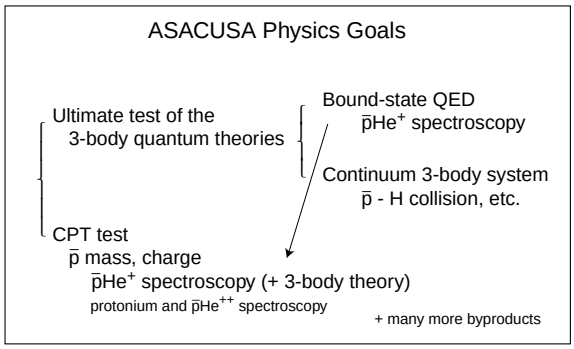

Figure 1: *The physics goals of ASACUSA.*

In 1997, when we presented our proposal to the SPSC[1], the precision achieved by our LEAR PS205

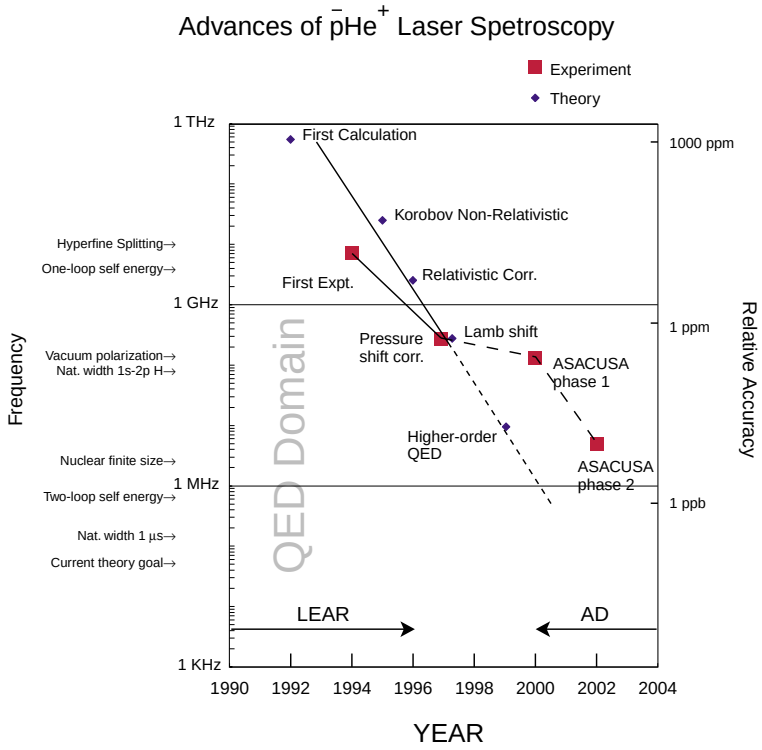

Figure 2: *The progress of theoretical and experimental precision on the antiprotonic helium transition energies over the past years. The interruption caused by the closure of LEAR and the opening of the AD is clearly visible as a kink in the experimental trend line.*

experiment for the $\overline{p}\mathrm{He}^+$ laser resonance[2] and the results of the quantum 3-body theories[3–5] were both in the range of ~ 1 ppm, as shown in Fig. 2. Since then, much progress has been made in the field of quantum 3-body QED calculations. In 1999, the theoretical calculations for $\overline{p}\mathrm{He}^+$ transition energies reached relative accuracies of 20 ppb, which will soon be improved to < 0.1ppb[6]. Such improvements on the theoretical side strongly motivates us to measure the $\overline{p}\mathrm{He}^+$ energy level spacings much more precisely than in the LEAR era. As can be seen in Fig. 2, we began LEAR PS205 with experiment well ahead of theory. Not surprisingly, if the trend lines of the figure can be believed, theory is now poised to take the lead over experiment for the first time in the history of the metastable antiprotonic helium atom. This constant interplay between theory and experiment is nevertheless to be expected and even welcomed – it was indeed the engine that drove forward our understanding of the hydrogen atom and its particulate components for almost a century.

1.2 Phase 1-2-3 Strategy

As shown in Fig. 3, ASACUSA will evolve in three phases. This plan was already presented to the SPSC in November 1997, when the committee fully approved the phase 1-part of our proposal.

In the first phase, we use the direct $\overline{p}$ beam from AD at 5.3 MeV and concentrate on the laser and microwave spectroscopy of $\overline{p}\mathrm{He}^+$. Our original plan, as shown in Fig. 3, was to complete the phase 1 experiments already in 1999. We have therefore been ready to use the AD beam for phase 1 experiments since Summer 1999. Due to the delay in the AD commissioning, we have been obliged to defer these experiments to the first half of 2000, encouraged however by the fact that during the last hour the 1999 beamtime we were able to reproduce at the AD, under extremely unfavourable conditions, the laser transition

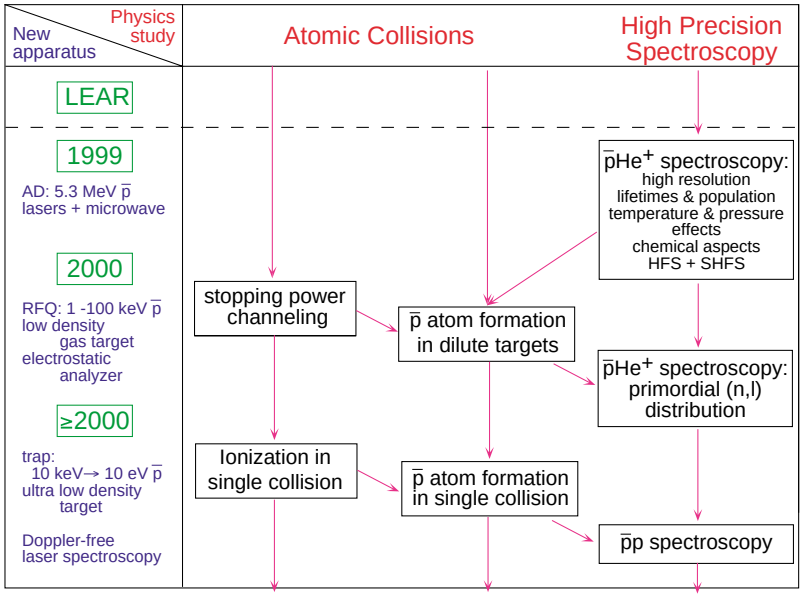

Figure 3: *The three phases of ASACUSA experiments, as presented at the SPSC meeting in November 1997.*

$(39, 35) \rightarrow (38, 34)$ found at LEAR in 1994 (Fig. 4).

In phase 2 experiments, now being formally proposed pending the success of the RFQD tests, we will add an RFQ linear decelerator, which decelerates antiprotons from 5.3 MeV to few tens of keV. This will enable us to study antiprotonic atom formation in very dilute gases, and will also make it possible to measure antiprotonic energy loss in various materials down to $\sim$ 1 keV (see Fig. 5). The RFQD has already been

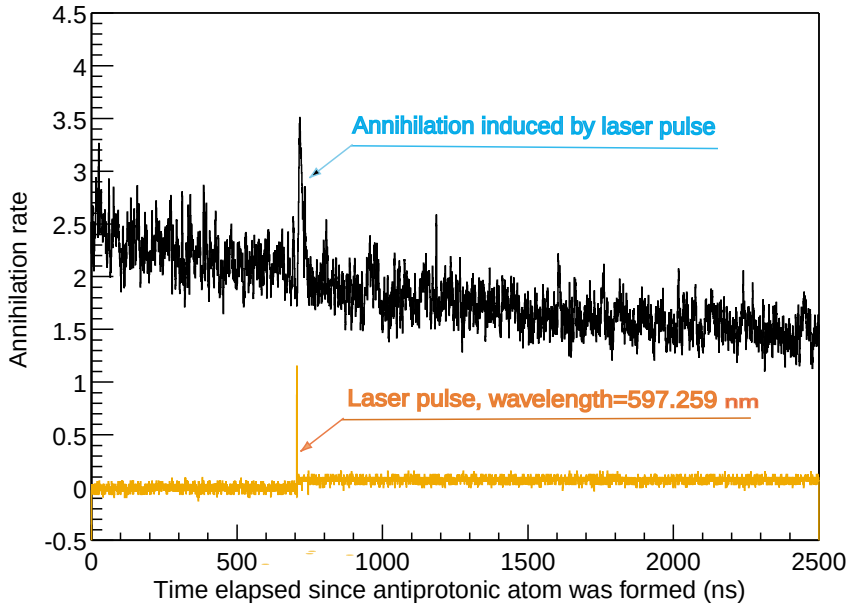

Figure 4: 597 nm resonance as observed at the AD in 1999.

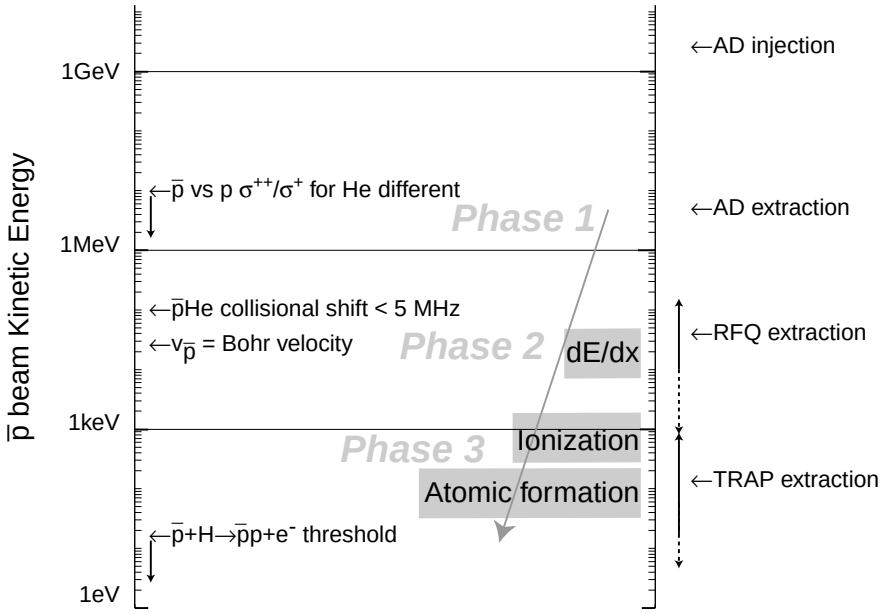

Figure 5: *Low energy antiproton beams to be used by the ASACUSA phase 1, phase 2 and phase 3 experiments.*

constructed, and will soon be tested at the Aarhus tandem. In section 3, we describe the RFQD status and our beam test timelines. When the PS division has completed its tests of the RFQD at Aarhus and at CERN, we shall submit to the SPSC a document describing the test results.

In phase 3, another powerful device, an antiproton trap will be installed downstream of the RFQD. Antiprotons will be captured and cooled (by collisions with electrons) in the trap, and will be extracted at and below $\sim$ 1 keV (eventually down to $\sim$ 10 eV). With such ultra low energy beam, hitherto never obtained, it will become possible to produce antiprotonic atoms in a single-collision environment, i.e., in $\sim$ vacuum, and to study their production mechanisms in detail, and also to perform high precision spectroscopy. Since we wish to install the trap in the AD hall in the fall of year 2000 and to start testing it, we have included the status of the trap construction and our beam test plans in the present proposal.

1.3 Plans for the Year 2000

Based on the draft schedule of the PS complex for the year 2000, we have made the following plans for the phase 1 and phase 2 experiments of the ASACUSA collaboration:

Period	Number of weeks	Our plans
Week 21 – 36	16 (incl. 2 weeks of AD SU/MD)	Phase 1 experiments and $\overline{p}\mathrm{He}^+$ phase 2 preparation
Week 37 – 39	3	RFQ, ESA and trap installation
Week 40 – 43	4	dE/dx measurement using RFQ + ESA
Week 44 – 48	4.4	Trap commissioning and test

2 Status report

In this section we describe the technical status of all components of the experimental apparatus for phase 1 experiments, and the construction of the RFQD.

2.1 Antiprotonic helium phase 1 preparations status

The first phase of measurements at the AD will consist of laser and microwave spectroscopy experiments of antiprotonic helium atomcules. In order to perform them, a cryogenic target capable of holding helium gas at temperatures of about 6 K and pressures between 200 mbar and 10 bar is necessary. This target chamber needs a window thin enough for the 100 MeV/c antiprotons from the AD to pass through, and a quartz window for the laser beam to enter. For the microwave experiment, the antiprotons must be stopped in a cavity supplied with microwave radiation through a waveguide leading to a room-temperature travelling wave tube amplifier. The annihilations of antiprotons in helium are detected by Čerenkov counters where the analog output signal of a specially designed gated PMT is recorded by a digital oscilloscope. Complex laser and microwave systems are needed to supply the required electro-magnetic radiation. The status of the technical preparations of the major components and the result of the few days of beam time in 1999 will be described in the following.

In the last days of November and the first days of December 1999, the AD team succeeded in extracting a beam of antiprotons to the three experiments. Due to the lack of electron cooling at 100 MeV/c (exactly 102.4 MeV/c), the beam quality was rather bad. At the DE1 focus in the ASACUSA area, a beam profile of 9 mm horizontally (FWHM) and 3 cm vertically was measured by a mobile wire chamber outside the beam line vacuum. Since the beam window has an aperture of about 3 cm, the beam size inside the vacuum pipe may have been even larger. The total intensity was estimated to about 10^5 $\overline{\mathrm{p}}$ in pulses of $\sim$ 600 ns length which arrived at about 2 minute intervals. In spite of this bad beam quality, we succeeded in the last few hours of the 1999 AD beam time in reproducing a laser resonance previously found at LEAR, which proves our readiness to perform the already approved experiments of phase 1 as soon as the AD beam becomes available in the year 2000.

2.1.1 AD beam window and beam profile monitor for 100 MeV/c

For our measurements the AD beam of 100 MeV/c momentum (5.3 MeV kinetic energy) has to be stopped in helium gas of typically 6 K and 500 mbar corresponding to a density of 6×10^{20} cm^{-3}. They have therefore to be degraded strongly, so that the beamline vacuum of the AD can be separated from the isolation vacuum of the cryostat by two windows and a short air gap. In order to keep the angular scattering as small as possible so as not to enlarge the beam size, the window and additional degrader have to be chosen carefully and placed as close as possible to the chamber where the helium gas is kept.

The best compromise between required thickness to withstand a pressure difference of 1 bar and minimal angular scattering of the beam turned out to be a Upilex (a polyimide similar to Kapton) foil. At a diameter of 4 cm required for the initial beam tuning, a thickness of 50 μm is enough to withstand the pressure. It has been tested by the PS vacuum group that such a window glued onto an aluminum vacuum chamber is acceptable also in terms of outgassing and permeability to air. A vacuum of 5×10^{-8} mbar could be reached easily by pumping with a small turbo molecular pump over several days. The window was installed in the ASACUSA beamline in November 1999.

The ASACUSA beam profile monitor (BPM) is a secondary emission chamber made of 0.5 mm wide aluminum stripes evaporated onto very thin polyimide foils. This type of chamber is gas-free and therefore windowless, and is mounted inside the AD beam line vacuum upstream of the 50 μm beam pipe window. The total thickness of all foils is only $\sim$ 5 μm. It has 16 x 16 channels, covering an active area of 8 x 8

mm^2, but can be enlarged to twice the size and number of channels if necessary. The stripes are read out via ultra-high sensitive pre-amplifiers and active filter post amplifiers with 2 μs time constant and digitized using CAMAC ADCs. The noise level of the pre-amplifiers is about 300 electrons (rms), and therefore has a sensitivity of a few hundred antiprotons per strip. Fig. 6 shows the profile of the AD beam at the DE1 focus as obtained with this secondary emission chamber in December 1999. Since the beam is larger than the active area of the BPM, only small variations can be seen over the detector size.

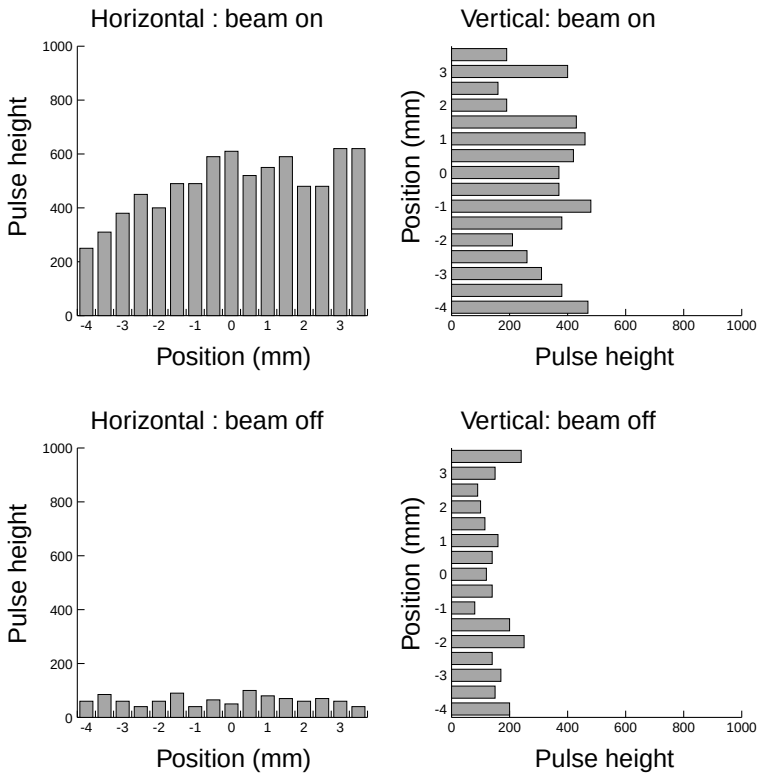

Figure 6: *(Top) Profile of AD beam at the focus of DE1 beamline, measured with the new ASACUSA secondary emission chamber. Beam intensity is some* 10^5 *particles/shot, and the diameter is much larger than the active area (8 mm* $\times$ *8 mm) of the detector, because the electron cooling at 100 MeV/c has not yet been set up; cross-measurements with CERN MWPC indicates a profile of 9 mm horizontal and 30 mm vertical. (Bottom) Without beam.*

2.1.2 Cryogenic target for high-density measurements with and without microwaves

Our measurements require a temperature range for pure helium gas or helium gas with admixtures between 6 K and 100 K, and a pressure range between 0.2 and 10 bar. For the phase 1 hyperfine structure measurement described in CERN SPSC 97-19, Section 2.6.3, a cylindrical cavity of inner diameter 28.3 mm and length 24.6 mm (see section 2.1.4) has to be inserted. The best solution we found was to use a cavity whose both ends were made of a metal mesh, fine enough to contain the microwave radiation inside, but coarse enough to let the antiprotons and laser light pass through. The helium gas is then held in a chamber surrounding the cavity. In order to minimize the distance the $\overline{\mathrm{p}}$ have to travel through helium gas between the entrance

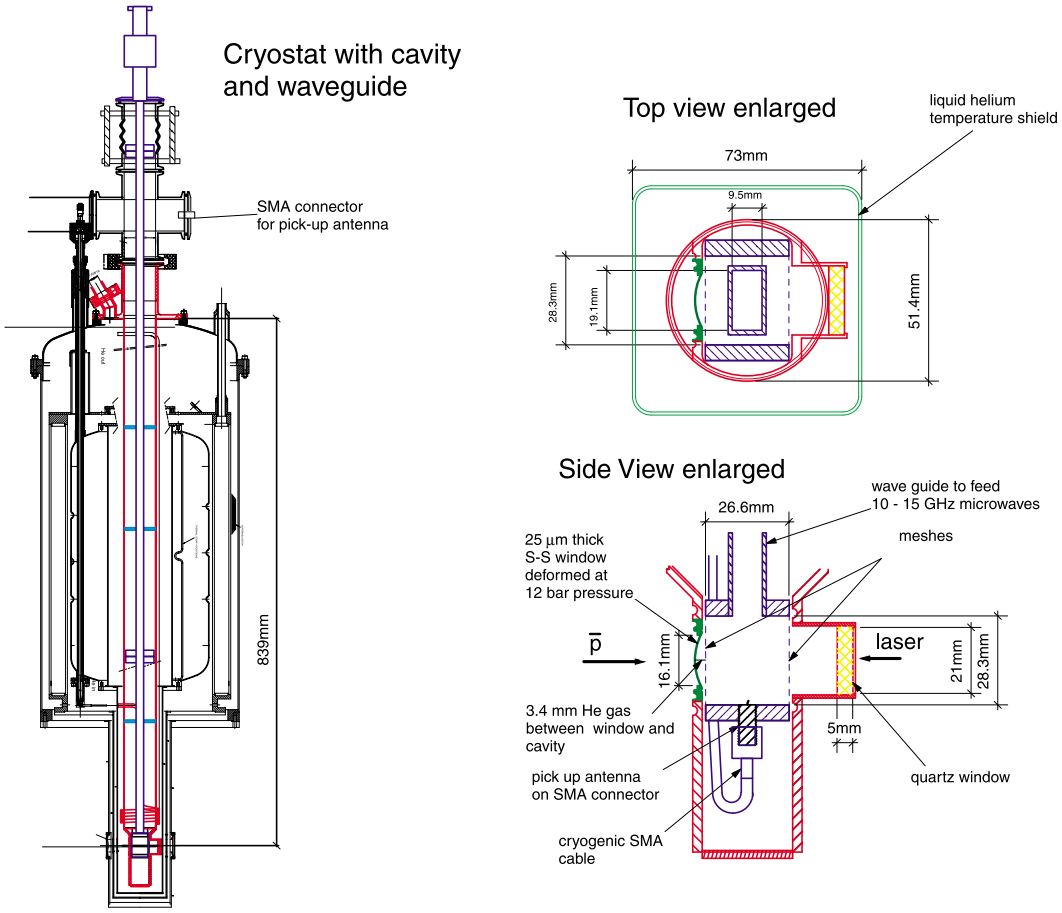

Figure 7: *Cryostat and inset to hold the microwave cavity.*

window and the start of the cavity, this chamber had to be designed to fit very tightly around the cavity.

Fig. 7 shows the cryostat and chamber. The cryostat itself was bought from AS Scientific in Oxford, UK, while the chamber to hold the helium gas together with a 51.2 mm diameter pipe to supply the gas and mount the cavity with its waveguide was designed and manufactured in the CERN workshops in close collaboration with the CERN cryogenics laboratory.

The chamber is supported and connected to the top of the cryostat by a 51.2 mm inner diameter stainless steel (316L) pipe of 1.2 mm wall thickness. This large diameter was required to insert the cavity with outer dimensions of 38.3 mm times 25 mm. The chamber itself was made by electro-erosion from a solid piece of stainless steel (304L) with a wand thickness of 3 mm.

The antiproton window was made of a stainless steel foil of 25 μm thickness. In order to minimize the distance between the metal foil and the cavity which needed to be inserted from above, the edges of the foil were bent and it was welded between two rings for support. The whole window was then connected by electron beam welding into the chamber. This type of window had been tested beforehand in the CERN main workshop to easily withstand pressures of more than 10 bar. At 10 bar a maximum plastic deformation of 1.5 mm was observed.

For the laser beam, a quartz window of 20 mm diameter attached to a short Kovar pipe was electron-beam welded into the chamber. This window was certified to withstand 10 bar pressure at temperatures down to 5 K.

The cavity is surrounded by two thermal shields at 4 K and 77 K, and a vacuum vessel. To minimize the distance between the window in the vacuum vessel and the chamber, the vessel was made square-sectioned with a length of 10 cm. The distance between the two windows could therefore be kept at ~ 38 mm. The outer $\overline{\mathrm{p}}$ window is made of 50 μm Upilex foil, like the window in the AD beam line.

The stopping distribution of antiprotons was calculated for this geometry by a Monte-Carlo program developed at the University of Tokyo that uses Ziegler's parametrisation of the energy loss of $\overline{\mathrm{p}}$ at low energies and also includes the Barkas effect. It was found that an additional degrader of 30 μm Upilex foil is needed to stop the pbar in the center of the cavity. A typical stopping distribution at 6 K and 50 mbar is 1 cm along the beam axis and 1 cm perpendicular (FWHM) for beam parameters as described in the AD design report (focus parameters: 1 mm horizontal and vertical size, and 30 or 7 mrad horizontal or vertical divergence, resp.) In the 1999 run helium gas of 6 K and 1 bar was introduced, dense enough to stop the $\overline{\mathrm{p}}$ without additional degrader. As mentioned above, the beam size was much larger (~ 1 cm horizontally and > 3 cm vertically). The majority of $\overline{\mathrm{p}}$ therefore did not enter the target chamber through the 16 mm diameter window, but stopped in the walls of the target chamber and the vacuum vessel of the cryostat.

The cryostat has been successfully tested in the CERN cryogenics laboratory with the cavity mounted inside. Due to the shortness of time in the 1999 run, no experiments with microwaves were possible and the cavity was not inserted. Instead a pipe holding several copper disks acting as baffles to reduce the heat radiation from the room-temperature region on the top of the cryostat was inserted into the stainless steel pipe.

2.1.3 Laser system

Two laser systems have been installed in a dedicated clean-room type laser hut in the AD hall. Both consist of a dye laser (Lambda Physik ScanMate 2E) pumped by a Nd:Yag laser (Coherent Infinity 15-30). One of the lasers is equipped with a frequency doubling unit to reach the UV, while the other has an OPPA extension making use of the optical parametric oscillator effect to extend the wavelength range to the infrared. All together a wavelength region of 260 nm to 1100 nm can be covered with a pulse energy of > 10 mJ.

After extensive practice, a band width of < 800 MHz could be achieved which is important to resolve the doublet structure of the 726 nm transition used in the hyperfine measurement. The wavelength is measured for each shot by a commercial interferometer ("Lambdameter" LM-007 from ATOS GmbH). This was calibrated against known absorption lines of iodine vapour and was found to be accurate at a level of less than 1 ppm. For the first run the laser was set manually to 597.263 nm, the value previously found for the 597 nm resonance line at a target gas density corresponding to 6 K and 1 bar. The Yag laser was triggered by a timing signal derived from the RF control signal of the AD, arriving ~ 380 μs before the antiprotons arrive at the target. The extraction from the AD occurred about every 2 minutes. We had already verified beforehand that an acceptable power fluctuation of ~ 10 % from shot to shot will occur under these conditions.

2.1.4 Microwave system for hyperfine structure measurements

As explained in our phase 1 proposal [1] section 2.5 and 2.6.3, an oscillating magnetic field of frequency $f = 12.91$ GHz with a strength of at least 3 Gauss is needed to induce transitions between the hyperfine levels of $\overline{\mathrm{p}}\mathrm{He}^+$. As also stated there, the central frequency of this cavity has to be tuned by about 1% without physically changing its size since it has to be kept inside a cryostat at liquid helium temperatures.

In the meantime a cavity has been designed and constructed to produce such a field. It is a cylindrical cavity with the axis parallel to the antiproton beam, oscillating in the TM110 mode. Both top and bottom sides consist of meshes in order to allow the $\overline{\mathrm{p}}$ and the laser beam to enter. The meshes are (like the cavity itself) made of stainless steel 304L with a "wire" width of 60 μm and a wire-to-wire distance of 0.744 mm. The thickness parallel to the beam is 0.3 mm. As indicated in Fig. 7, it is connected by a waveguide made of

stainless steel with a 10 μm thick layer of copper on the inside so that the high-frequency radiation will not be attenuated too much. A pick-up antenna inside the cavity is connected to the outside by a special coaxial cable which has a small thermal conductivity and a small attenuation of the microwaves by using a central conductor made of a thin pipe of stainless steel, again covered by a few μm of copper.

The cavity is coupled to the wave guide in a way that the resulting loaded Q-value is much smaller ($Q_L^C = 96.5$) than the intrinsic Q-value of the cavity ($Q_0^C = 2700$) ("overcoupling"). Outside the cryostat, a triple stub tuner (TST) is inserted in the waveguide. It consists of 3 pieces of waveguide perpendicular to the main waveguide, situated at a distance of 3/4 of a waveguide wavelength. Inside the three waveguide extensions, movable metal pieces are placed which act as a short-circuit for the microwaves. By moving the shorts using computer-controlled stepping motors, the impedance matching between the TST and the system cavity plus waveguide can be changed, thus modifying the central frequency and total loaded Q-value Q_L.

The right side of Fig. 8 shows the reflection (S11) and transmission (S21) curves as measured with a vector network analyzer for two different positions of the TST leading to different central frequencies. The difference of 22.3 MHz is close to the theoretically predicted difference of 27.97 MHz between the two allowed transitions within the hyperfine quadruplet of $\overline{\mathrm{p}}\mathrm{He}^+$ (cf. Fig. 8 left). The total Q-value given by the "sharpness" of the resonance curve ($Q = f_c/\Delta f$, where Δf is the width (FWHM) of the resonance curve) in both case is $Q_L \sim 3000$. Extended simulations of the cavity by the three-dimensional code HFSS (Hewlett-Packard/Ansoft) showed that at a Q_L of 2000 a maximum magnetic field with ~ 50 Gauss is generated using a pulsed traveling wave tube amplifier (TWTA) of 2 kW power as we have purchased. We therefore have demonstrated that we can produce a strong enough magnetic field over the tuning range required with our method.

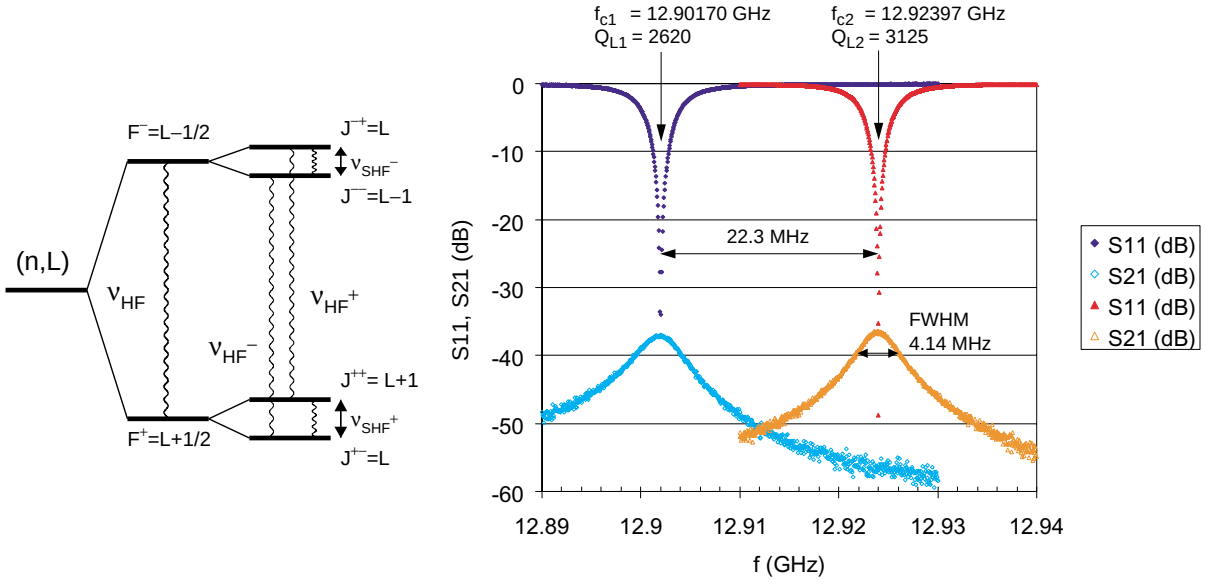

Figure 8: *Left: level splitting of $\overline{\mathrm{p}}He^+$ into a quadruplet due to the interaction of $\overline{\mathrm{p}}$ angular momentum L, electron spin and $\overline{\mathrm{p}}$ spin. For the (37,35) state the allowed transitions are predicted to be at $\nu_{\mathrm{HF}}^- = 12.9239$ GHz and $\nu_{\overline{\mathrm{HF}}}^- = 12.8958$ GHz [7], resulting in a splitting of $\Delta\nu_{\mathrm{HF}} = 27.967$ MHz. Right: Resonance curves at 2 different positions of the triple stub tuner around the above-mentioned frequencies.*

2.1.5 Čerenkov counters to detect delayed annihilation of antiprotonic helium

The delayed annihilation of antiprotonic helium atomcules is measured as before at LEAR by recording the analogue output signal of a photo multiplier tube (PMT) connected to a Čerenkov counter. A Čerenkov counter is used because of its fast time response in contrast to scintillation counters which have long decay components. The PMT needs to be gated so that it will not be saturated by the large flash of light coming from the 97 % prompt annihilations during the antiproton pulse.

For the AD a small Čerenkov counter (15 cm x 30 cm, 2 cm thick) was built out of special UV transparent high-purity lucite, optimized for a high photon collection efficiency. A new gated fine-mesh PMT of 1 inch diameter was developed by HAMAMATSU Photonics with highly suppressed after-pulsing immediately after the end of the gate pulse. The result of about 70 AD shots from the 1999 run added up is shown in Fig. 4. Using the same timing signal from the AD RF-system that served to trigger the laser, the PMT output was suppressed during the AD pulse of ~ 600 ns duration. The gate pulse ended ~ 300 ns after the end of the AD pulse.

The time spectrum (upper curve) shows a very linear structure even immediately after the gate pulse ($t = 0$ corresponds to the center of the AD pulse). Clearly visible although at still low statistics is a peak in coincidence with the arrival time of the laser light (indicated by the lower curve). The laser was tuned to the known wavelength of the 597 nm resonance for the corresponding density. The intensity of this laser resonance is only about 10 % of the value previously observed at LEAR, because, due to the large beam size, the majority of $\overline{\mathrm{p}}$ did not stop inside the helium gas. Those antiprotons annihilate and give rise to a background component in the time spectrum which comes from $\pi^+ \rightarrow \mu^+ \rightarrow e^+$ decays of pions stopped in the surrounding material. This component has the muon lifetime of ~ 2.2 μs, which is similar to the average lifetime of $\overline{\mathrm{p}}\mathrm{He}^+$.

In summary, the successful observation of a previously discovered laser resonance, even though at low statistics, has demonstrated that our experimental technique in principle is working. After the anticipated improvement of the AD beam quality to the status as described in the design report we will be able to pursue the full research program as described in our proposal [1].

2.2 Radio frequency quadrupole decelerator construction[1]

2.2.1 Supplements to the design report

Continued development after the approval of the radio frequency quadrupole decelerator project (RFQ for short) led to several changes with respect to the initial proposal. The most important are:

positioning the RFQ electrodes at 45 degrees (see figure 9). The dipole component of the RFQ-field is substantially reduced due to the balancing of the RF current path lengths as compared to horizontal/vertical electrode pairs. Also the manufacture of the ladder is simplified. This rotation is possible since the input and output beams are nominally "round", with correction if necessary in the upstream beam line. Figure 9 also shows newly added corona-shields at the top and bottom of the ladder, together with the insulating ladder support cylinder.

redesign of the low-energy beam transport LEBT (see rightmost part of figure 10). Instead of the original triplet at the RFQ output there is now a solenoid that makes the beam nearly parallel, followed by a second solenoid at the end of the LEBT that focuses the beam into the physics experiments. The intermediate space is used to mount a diagnostic box (carrying a retractable Faraday cup and a large pumping port), a SEM wire chamber (permanently in the line since 95% transparent to the beam, called HORI-box after its designer) together with vacuum valves and a pair of magnetic steerers.

[1] This section written by W. Pirkl, CERN PS division.

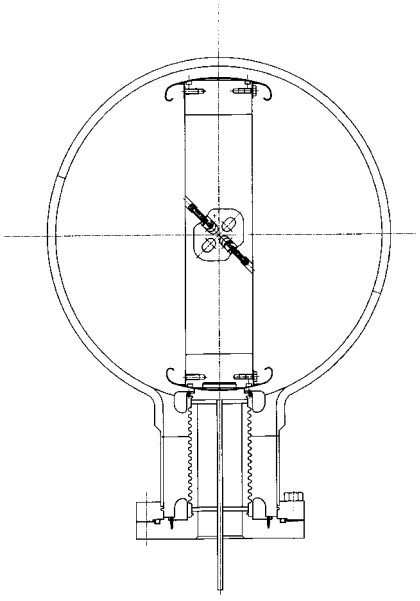

Figure 9: *Cross section of RFQ cylinder, showing ladder with electrodes under 45 degrees, corona shields and ceramic insulating support.*

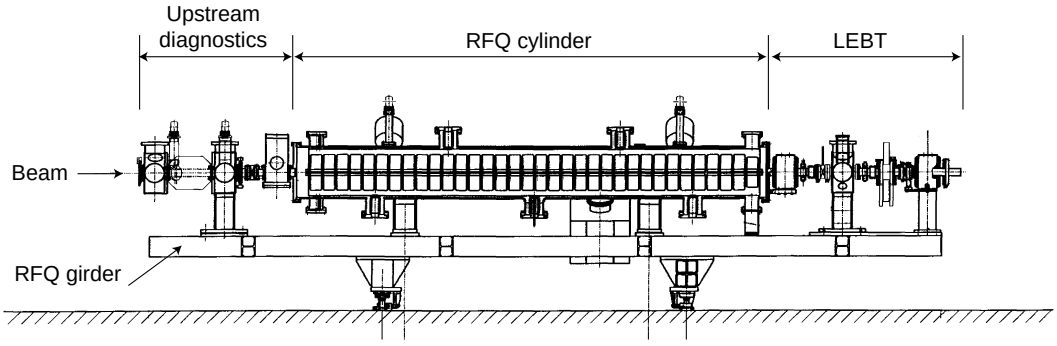

Figure 10: *General Assembly drawing of the RFQ girder with upstream diagnostics (left), RFQ cylinder (mid) and LEBT (right).*

redesign of the vacuum system. The LEBT is now equipped with a powerful pump assembly, consisting of a turbo pump 250l/s, an ion pump 125 l/s and a sublimation pump of 2000 l/s. It capitalizes on the small aperture of the RFQ output to provide differential pumping. The gas flow from the experiments to the RFQ (ASACUSA phase 2) respectively from the RFQ to the cryogenic solenoid (ASACUSA phase 3) is more efficiently reduced.

revision of the test method for the initial evaluation of RFQ performance. The initially proposed test method by electrons of the same velocity as the antiprotons has been abandoned. Extensive tests have shown that the extreme sensitivity of very-low-velocity electron beams to magnetic stray fields leads to unreliable measurement results. It has therefore been decided to come back to the alternative solution mentioned in the design report, namely to carry out the acceptance tests with a high-

quality proton beam available from the Tandem generator at the Institute of Storage Rings Facilities in Aarhus/Denmark (see also 2.2.3 below).

2.2.2 Present status

All parts of the RFQ and its girder have been received, installed and vacuum tested (see fig 11). The RF chains for the RFQ and the two auxiliary cavities have been installed and commissioned. Virtually all components and modules of the upstream diagnostics and of the LEBT have been delivered and tested.

Figure 11: *RFQ seen from downstream end, cover removed. In the background the RF amplifier.*

A dedicated beam test line has been designed, installed and calibrated. It consists of a 20-degree spectrometer magnet, a triplet and diagnostic equipment. This assembly is intended for the future RFQ acceptance tests and has been calibrated with a low-intensity 60 keV proton beam of known parameters. A second SEM wire chamber ("HORI"-box) is used as beam profile monitor of very high sensitivity. The output beam profile was initially checked at higher beam intensity using a standard SEM wire chamber and a microchannel plate followed by a scintillator screen.

A series of low level RF measurements were carried out. The measured resonant frequency, and in parallel the field pattern, differed from the predictions obtained from the RFQ design method which considers unmodulated electrodes together with analytical formulae to correct for the effect of the modulation. The differences can be explained by the important length of this particular RFQ; it makes the structure very sensitive to slight local tuning variations, while it reduces at the same time the resolution for a full-length simulation due to a practical limit on the number of available meshpoints.

Series of much extended 3D simulations have been carried out for each of the 34 RF cells. An electrostatic program module for evaluation the capacitance of the modulated electrodes, in conjunction with the RF module for the rest of the geometry, allowed precise determination of the individual cell resonant frequencies. In parallel the experimental setup was extended by mounting of a pair of movable tuning plates in each cell for modification of the local resonant frequency over a wide range. Adjustment of these plates led to excellent field flatness, albeit at higher than nominal frequency. Excellent correlation with the theoretical results was obtained.

The Q-factor of the assembly is lower than expected, resulting in larger than anticipated RF power requirement. Two actions have been started: On the one hand a single-cell resonator was built to study different means of loss reduction; in particular increased surface polishing has led to very encouraging results. On the other hand, an additional drive amplifier is being installed to deliver the additional power with some reserve.

2.2.3 Future plans

The RFQ ladder will soon be re-machined at CERN to achieve flat field at the correct frequency. This operation concerns only the relatively low-precision RF chamber heights, whereas the high-precision electrode seats will remain untouched. The tests with the tuning plates have built confidence in the theoretical predictions to a point where machining could start immediately. However the results of the Q-factor improvement may have a slight influence on the present geometry therefore the machining is foreseen for January 2000.

The full power test with the newly machined RFQ structure will be carried out during the CERN shutdown which lasts up to April 2000. During this period notable manpower limitations have to be taken into account.

The next step is the RFQ acceptance test with beam at Aarhus. The test setup is shown schematically in figure 12. It consists of

the upstream beam line which will essentially put at disposal by Aarhus. Tests have confirmed the excellent beam quality in the central line that has kindly been reserved for the RFQ tests.

the RFQD assembly i.e. the complete girder as shown in figure 10.

the measurement line, as described above.

The entire RFQ equipment will be completely tested before shipment, in a layout similar to the layouts in Aarhus and the AD hall. Connections are connectorized wherever possible. The test line is mounted on a self-contained girder that carries provisions for rapid and precise alignment with respect to the RFQ-girder. The net duration of the beam tests has been estimated at about one week.

The RFQ shall be back at CERN in due time for installation in the AD machine, which is foreseen from 11 September 2000 on.

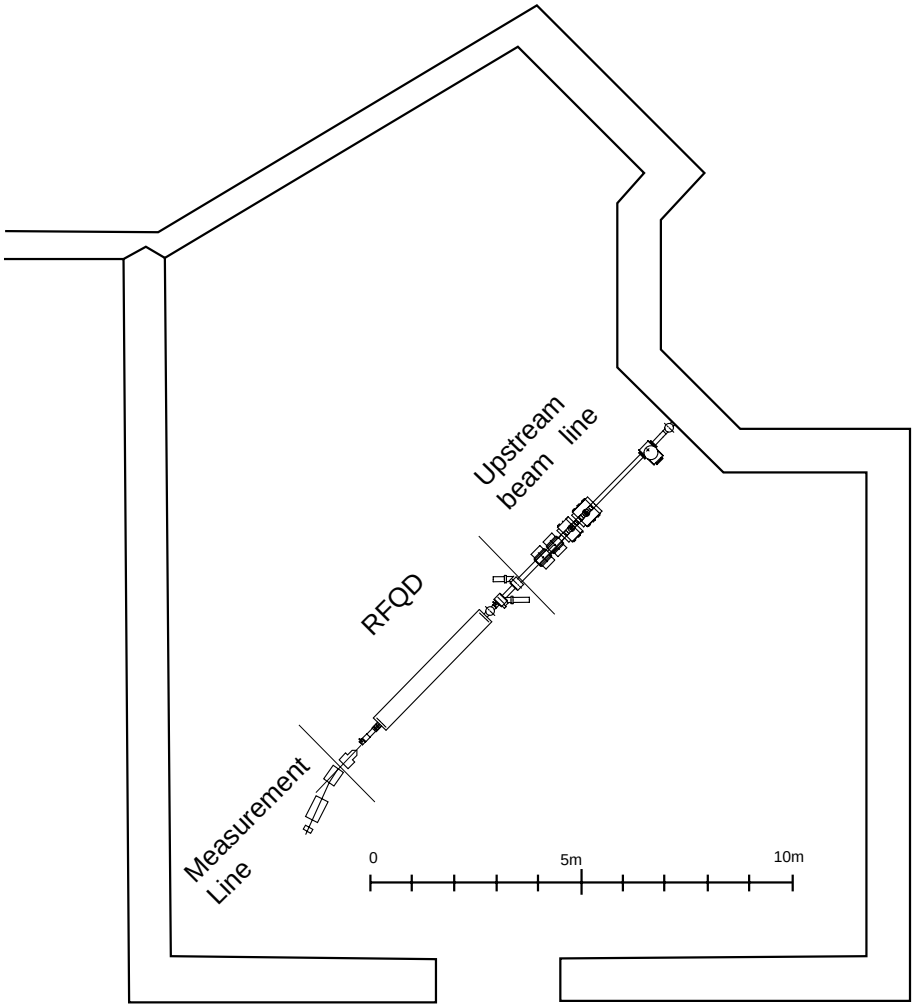

Figure 12: *RFQ test setup at the Institute of Physics and Astronomy, University of Aarhus, Denmark.*

3 Phase 2 experiments

In this section we describe not only the status of the phase 2 experimental hardware, but also go into the physics justification of some of the phase 2 experiments in somewhat more detail than was possible when we wrote our original proposal (CERN SPSC 97-19).

3.1 Measurement of $\overline{p}$ energy loss at very low energies

The stopping power of matter for charged particles is of large fundamental and applied relevance. Generally, it is of great importance to know accurately the stopping power for a broad range of materials and particles in order to interpret a variety of contemporary experiments. This holds true both directly and indirectly. Directly, *e.g.* in order to predict the response from a detector for a given particle beam incident with a given energy and indirectly, *e.g.* in order to predict the energy of a particle beam after the passage of a given material. Examples of widespread applications in industrial as well as fundamental science are radiotherapy, ion-implantation for semiconductors and ion beam analysis.

One of the measurements to be performed under the ASACUSA collaboration is a thorough investigation of the so-called Barkas effect in stopping power. In the late fifties Barkas and his collaborators found that negatively charged pions penetrating through matter had a slightly longer range than positively charged ones of equal velocity[8]. This was understood as a polarization effect where – since the main energy loss mechanism at high energies is scattering off electrons – the electrons are rejected from a negatively charged projectile and attracted to a positively charged projectile leading to a difference in the stopping power. However, as it is expected, the electrons need time during the passage of the projectile to accommodate to the field leading to the polarization, such that the effect is small at high energies and rises to a maximum near the typical velocity of the electrons in the medium, around the Bohr velocity, αc.

A similar polarization effect is seen in the ionization and excitation of atoms and molecules where the cross sections with projectile velocities near αc differ significantly for *e.g.* protons and antiprotons, being larger for protons. Nevertheless, in this case the roles are interchanged when projectile velocities somewhat below αc are used. Here, antiprotons excite and ionize more efficiently than protons because excitation and ionization requires close encounters, and the negatively charged projectile is attracted to the nucleus and thus spends more time in the vicinity of the electrons, an effect usually referred to as the Coulomb-trajectory effect. Furthermore, the approach of a (negatively charged) antiproton to the target atomic nucleus will lead to a decreased binding of the target electrons, thus increasing the probability for excitation/ionization, while the opposite effect is found for proton impact. This is called the binding/antibinding mechanism.

The Barkas effect was investigated by the PS194 collaboration at LEAR where the energy loss of protons and antiprotons in various thin foils of Z = 13, 14, 22, 29, 47, 73, 78 and 79 were measured in the energy range 30 keV – 3 MeV[9], see figure 13. This was done by a time-of-flight (TOF) technique where the speed of the projectile was measured before and after the target. Such a technique is only possible for a slowly extracted beam where each antiproton can be measured separately since the TOF must be determined to an accuracy of a few hundred picoseconds. To get sensible results, it is required to have thin, homogenous foils with a precisely known thickness which was measured by Rutherford backscattering.

We propose to extend the energy-loss measurements to much lower energies, by using the RFQ and electrostatic analyzers (ESAs), as described below. With the proposed setup, it will be possible to cover the energy range of $\sim$ 1 keV – 50 keV for solid targets, and it should be even possible to go down to ~ 100 eV with a gas target. At these very low energies, the nuclear stopping effect – the energy transfer to the target atoms as a whole – becomes important. Effects similar to the Coulomb-trajectory and binding/antibinding effects for ionization/excitation may also appear. Here we benefit from using antiprotons – 'the theorists favorite low-energy projectile' where effects of electron capture are avoided – to investigate stopping at low energies. Another aim is to investigate the region of applicability of the so-called electron-gas model, where

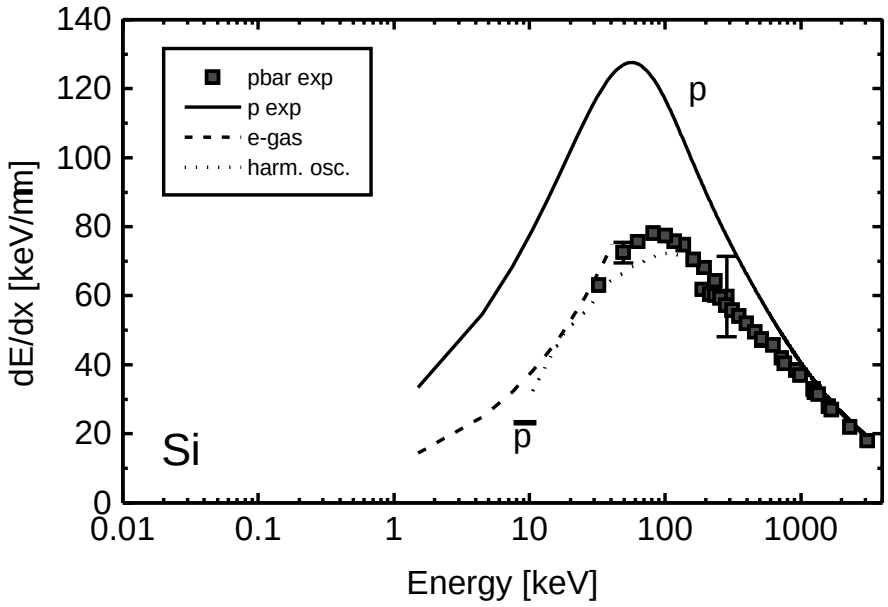

Figure 13: *Stopping power for protons and antiprotons in silicon.*

the stopping-power is calculated as taking place in an electron gas without reference to the nuclei present (dashed curve in Fig. 13).

3.1.1 ElectroStatic Analyzer

As the AD is not foreseen to operate in a slow extraction mode a new technique to measure the energy loss of bunched antiprotons must be invoked. The energy of the antiprotons incident on – and exiting the foil or gas is determined from the deflection in electrostatic analyzers (ESAs). By combining the ESAs with the RFQ, an average energy loss can be found by selecting *e.g.* 1000 antiprotons per shot in a well-defined incident energy range. Figure 14 shows a schematic top view of the ESA under construction[10], which comprises two 90° electrostatic deflectors. With the curvature radius of 250 mm, each deflector has an energy dispersion of $D = 5\mathrm{mm}/\%$ and the detector resolution of $\leq 0.2\mathrm{mm}$ thus gives a determination of p to better than 0.4%. Table 1 summarizes ESA parameters, and Appendix B gives a detailed design note of the ESA.

At the time of writing, all the pieces for the ESAs have been made and pumps, connectors and detectors have been bought. Assembly of the apparatus is foreseen to take place in January 2000 and tests with 60 keV protons will be done in spring 2000. The ESAs will be calibrated by means of protons or electrons, before they are shipped to CERN.

3.1.2 Target

The ESA can accommodate both solid and gas targets. For solid target elements, self-supporting foils as thin as 100 Å can be prepared, which effectively limits the lower energy to about 1 keV since the energy loss, ΔE, must be significantly smaller than the incident energy, E. To be able to investigate even lower energies where nuclear stopping – the energy transfer to the target atoms as a whole – becomes important, it is necessary to use gas targets. In this case it is intended to use a differentially pumped gas target of 100 mm extension., and with two windows confining the gas. Windows, 3 mm in diameter, will be made of 500

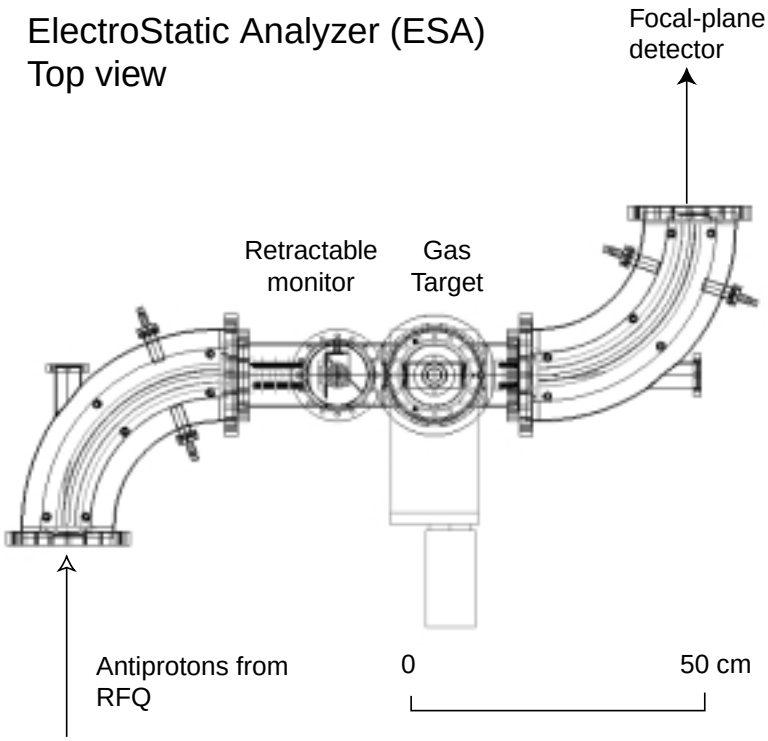

Figure 14: *Top view of the electrostatic analyzer.*

Table 1: Choices of ESA parameters.

Parameter	Value
Beam energy	0–120 keV
Gap distance	20 mm
Electrode height	60 mm
Potential difference	0 – 16 kV
Curvature radius	250 mm
Gas cell length	100 mm

Å aluminum or carbon, and the target gas pressure will be typically 10 mbar. With the use of gas targets we expect to be able to investigate stopping powers down to incident energies of the order 100 eV.

3.1.3 Particle detection and diagnostics

A retractable phosphorized channel-plate screen with a camera will be placed in front of the target, in order to diagnose the beam impinging on the target. Another channel-plate screen will be placed at the last focal plane of the ESA (see Fig. 14). The focal-plane camera has a frame grabber, so that the particle position resolution of about 0.2 mm will be achieved after off-line data analysis. Furthermore, as the number of particles which appear at the focal-plane detector may be quite small for the low-energy measurements, the number of particles can be obtained simply by digitizing the pulse height of the channel plate.

Table 2: Selected antiproton energies and their energy loss, simulated transmission, output sensitivity, energy straggling, multiple Coulomb scattering and emittance increase ($\beta = 5$ cm) for a 0.05 mm Al foil.

E [keV]	ΔE [keV]	τ [10^{-7}]	δ [keV/cm]	Ω [keV]	θ [mrad]	$\Delta\epsilon$ [π mm-mrad]
1	0.61	50	0.10	0.20	2076	107700
2	0.86	100	0.17	0.23	1038	26960
5	1.4	250	0.31	0.29	415	4312
10	1.9	490	0.45	0.35	208	1078
20	2.7	880	0.66	0.42	104	269
50	4.3	1400	1.1	0.52	42	43
80	5.5	1590	1.4	0.59	26	17
100	6.1	1630	1.5	0.62	21	11

3.1.4 Measurement Scheme

Assuming an efficiency for the extraction from the AD combined with that of the RFQ to be 50% with one extraction per minute, we get 720 shots per day. We propose to measure at (1, 2,) 5, 10, 20, 50, 80 and 100 keV, each measured point consisting of a 'scan' around the most probable energy loss, if possible to determine the energy straggling. Each 'scan' consisting of 10 points it can be expected to finish one foil or gas in a couple of hours. Thus, three-four days of dedicated running would be enough for the measurement (under these somewhat optimistic assumptions), excluding time for the setup and initialization. Table 2 shows the precision and count rates that can be expected from a 500 Å aluminium foil.

3.2 Antiprotonic helium atom studies in low-density helium

The low-energy antiproton beam ($20 - 100$ keV) of the RFQ allows for stopping of $\overline{\mathrm{p}}$ in helium gas of much lower density than the direct 5.3 MeV beam of the AD or the beam previously available at LEAR. The production of $\overline{\mathrm{p}}\mathrm{He}^+$ atomcules in low-density medium is of greatest importance to *i)* high-precision studies of transition energies, since the influence of collisions on the shift and width of resonance lines is highly reduced, and *ii)* studies of initial populations, where some primordial population may become visible which is destroyed at higher densities. Both topics will be discussed in greater detail in the following sections.

3.2.1 Preparation status

As described in our proposal [1] section 3.1, we will use a cryogenic helium target of about 6 K and 5 mbar. The use of low temperature gas is mainly chosen to exclude the influence of any contaminants which will be frozen at that temperature. This is especially important since due to the low energy of the $\overline{\mathrm{p}}$, the window of the target chamber has to be made out of ultra-thin (200–300 nm thick) Collodion foils which may considerably outgas. Fig. 15 shows the dedicated low-density cryostat which is already constructed and awaits first cool-down tests at the CERN cryogenic laboratory. Without the inner chamber that eventually will hold the helium gas, the cryostat has already been tested for vacuum and after baking at 200 °C for 24 hours, a vacuum of 1×10^{-9} mbar could be achieved. After mounting the target chamber, the ultimate vacuum (which must not exceed 10^{-6} mbar so as not to contaminate the RFQ vacuum) will be dominated by the leakage of helium through the Collodion window. Tests at room temperature at the University of Tokyo showed that a vacuum of 1×10^{-8} mbar could be achieved on the outside of a 200 nm thick Collodion window when 10 mbar of helium gas were kept on the other side.

The stopping distribution of the low-energy antiprotons in the dilute gas has been simulated (as already described in the proposal) by a Monte-Carlo program that uses experimental data for the stopping power of $\overline{\mathrm{p}}$ at energies of 1 – 100 keV in helium gas and thin films, as measured by the OBELIX [11, 12] and PS194 [9] collaborations at LEAR, and includes the treatment of energy loss and multiple scattering according to the Vavilov and Moliere distributions, resp. The results as shown in Fig. 16 indicate that the antiproton beam will stop within a 4 – 6 cm spherical region in the helium gas target at 6 K and 5 mbar. The target chamber of

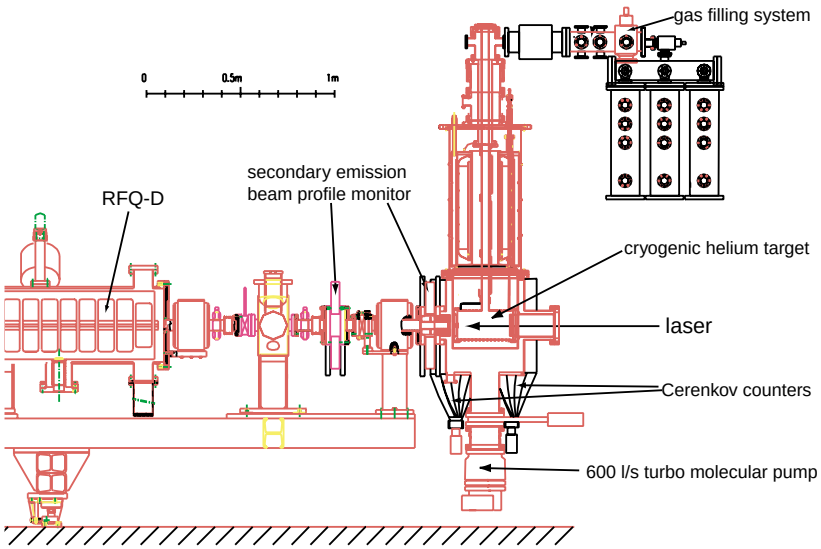

Figure 15: *The low-density target connected to the low-energy beam transport (LEBT) of the RFQ.*

the low-density cryostat is therefore a cylinder of 150 mm diameter and 300 mm length, equipped with 100 mm clear view windows for the laser beam made of 15 mm thick high-purity UV-transparent fused silica.

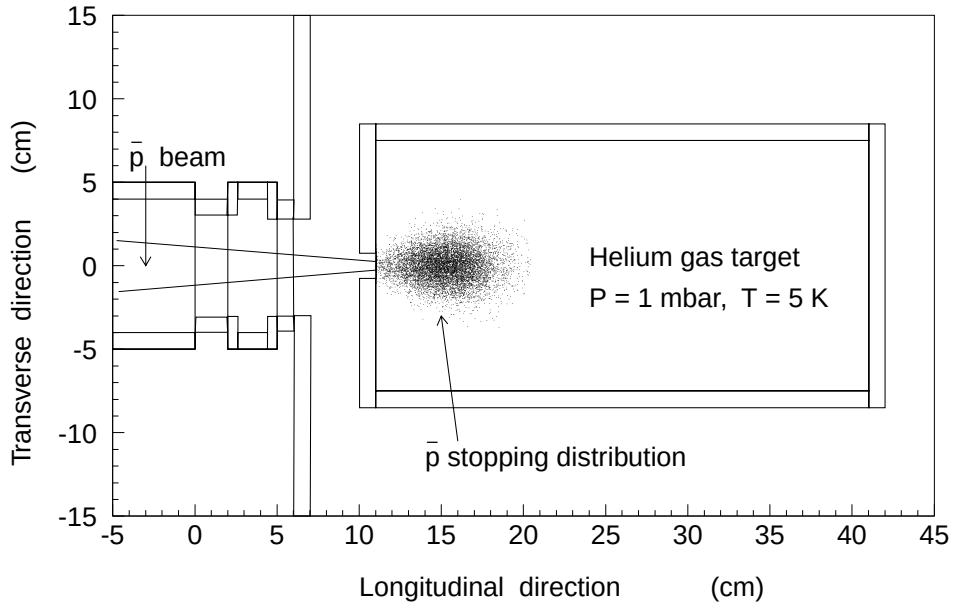

Figure 16: *A cross section of the cryogenic helium target, showing the spatial distribution of $\overline{\mathrm{p}}He^+$ atoms obtained from a Monte-Carlo simulation for a temperature of 5 K and a pressure of 1 mbar corresponding to a density of $\rho \sim 10^{18}$ cm^{-3}.*

Also shown in Fig. 15 is a secondary emission beam profile monitor (BPM) situated between the LEBT of the RFQ and the low-density cryostat. Identical BPMs are used inside the LEBT to measure the antiproton beam properties. A photograph of the BPM can be seen in Fig. 17 (left). It uses the same amplifiers and readout as the phase 1 BPM described in chapter 2.1.1, but uses 10 μm thick Tungsten-Gold wires with a spacing of 0.25 mm instead of the aluminum strips evaporated onto polyimide films. It therefore destructively intercepts only 1% of the keV antiprotons. The active area of the detector is 30 x 30 mm^2. It is constructed using ultra-clean semiconductor manufacturing techniques, can be baked to 200 °C and is compatible to a vacuum level of better than 10^{-11} mbar. The BPM has been successfully tested at the 50 keV Duoplasmatron proton source of the PS division at CERN together with the other components of the LEBT (Fig. 17 right).

3.2.2 Higher resolution spectroscopy

At the end of LEAR, the laser spectroscopy of antiprotonic helium by the PS205 collaboration had reached an accuracy of 0.5 ppm [2]. At the time of the submission of our initial proposal [1], the most advanced 3-body theories [3–5] were able to calculate the energy levels of $\overline{\mathrm{p}}$ with similar precision. Since the values for the proton mass and charge are used for the antiproton in the calculations, the comparison of experimental and theoretical results allows to impose constraints on these fundamental properties of the antiproton. This constitutes a CPT test under the assumption that the calculations are correct to the respective level of precision. The final result for the equality of proton and antiproton charge and mass were [2]

$$\frac{|Q_{\overline{\mathrm{p}}} - Q_{\mathrm{p}}|}{e} < 5 \times 10^{-7} \quad \text{and} \quad \frac{|M_{\overline{\mathrm{p}}} - M_{\mathrm{p}}|}{M_{\mathrm{p}}} < 5 \times 10^{-7}\,, \tag{1}$$

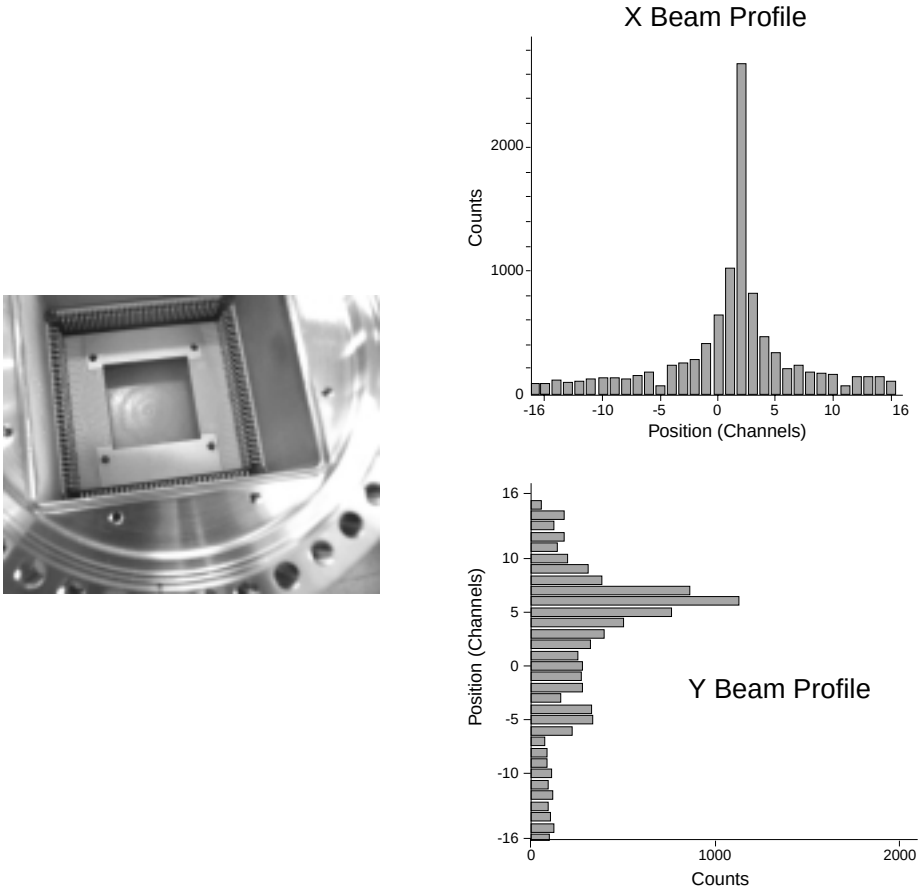

Figure 17: *Left: ASACUSA secondary emission chamber: a non-destructive antiproton beam monitor to be used at the exit of the RFQ. Right: first beam profile of a 50 keV pulsed proton beam (intensity* 5×10^5 *protons, pulse width 2* μ*s) at the CERN-PS Duoplasmatron source.*

two orders of magnitude better than the previous values published by the Particle Data group [13].

This result shows the potential of this exotic three-body system $\overline{\mathrm{p}}\mathrm{He}^+$ of studying the fundamental properties of the antiproton and thus the CPT theorem. Furthermore, it also allows to test bound-state QED. Already at the level of 0.5 ppm the calculations have to include the largest QED correction, the Lamb shift, in order to agree with our results. In the meantime, the theory has made further progress, and the most recent calculation of Korobov [6] has reached an accuracy of 20 ppb for the transition energy of the $(n, l) = (39, 35) \rightarrow (38, 34)$ transition at 597.26 nm (n being the principal quantum number, and l the angular momentum quantum number of the $\overline{\mathrm{p}}$ state). In addition to the Lamb shift, the next-order QED corrections (vacuum polarization and two-loop corrections), and nuclear finite-size corrections have been calculated. The dominating error of the theoretical calculation, however, comes from the Auger width of the (38,34) daughter state. It should be noted that at this level of precision the hyperfine splitting of the levels due to the interaction of electron spin and antiproton angular momentum has to be taken into account. The measurement of this splitting constitutes a central experiment in the phase 1 of ASACUSA. Korobov estimates that a relative theoretical accuracy of 0.1 ppb for the transition energies can be reached in the "not-so-far future".

The achievable accuracy in phase 1 using the 5.3 MeV beam of the AD is limited to about 0.5 ppm by the factors listed in Table 3. They originate from the presently employed laser system, but also from the

high density of helium gas needed to stop the 5.3 MeV antiprotons. A significant improvement can only be obtained by

1. the use of low-energy antiprotons that can be stopped in low-density helium gas,
2. Doppler-free two-photon spectroscopy, and
3. a new laser system with significantly reduced bandwidth.

By using the low-density cryostat with helium gas of about 6 K and 5 mbar or less, the collision-induced shift and broadening of the transition lines can be reduced significantly. Extrapolation of the measured shift for the 597.26 nm and 470.72 nm resonances yields a typical value of ≤ 50 ppb under these conditions. In a similar way the collision-induced broadening can be estimated to become smaller than ~ 5 MHz.

The Doppler-broadening of 0.5 GHz at 6 K due to the thermal movement of the atomcules can be reduced by employing a two-photon spectroscopy method where two counter-propagating photons are used to induce a transition, thus cancelling the Doppler-shift due to the movement of the atomcule. In addition to the classical method of making a $\Delta n = 2$, $\Delta l = 0$ transition with two photons of identical wavelength, it is also possible to use $\Delta n = 2$, $\Delta l = 2$ transitions. In this case the intermediate virtual level can be brought close to a real level, which greatly enhances the transition probability, or vice versa reduces the required power to saturate the transition, as described in section 4.2.4 of our first proposal. Calculations show that a pulse energy density of 20–40 mJ/cm^2 and therefore a pulse energy of ~ 100 mJ are needed to saturate a $\Delta n = 2$, $\Delta l = 2$ transition, a factor 2-4 less than for a $\Delta n = 2$, $\Delta l = 0$ transition.

Fig. 18 shows two candidate transitions, one of which (a) includes two already observed transitions at 470.72 nm and 529.62 nm. This way we can be sure that significant population exists in the parent state of the two-photon transition $(38, 35) \rightarrow (36, 33)$. The other (b) uses two transitions between exclusively metastable states $(36, 35) \rightarrow (34, 33)$ followed by a broadband single-photon transition to a shortlived state $(34, 33) \rightarrow (35, 32)$. In this case the width of the 2-photon transition much smaller than in (a) due to the much longer lifetime of the metastable daughter state $(34, 33)$ as compared to $(36, 33)$. The required wavelengths of 498.44 nm and 391.42 nm as well as the pulse energies lie in a comfortable region for pulse-amplified cw laser systems like seeded dye lasers or the frequency-doubled output of an Alexandrite laser seeded by a cw Ti:S laser.

The remaining limiting factors when using such a high-resolution laser system and low-density helium gas are listed in Table 4. The AC Stark effect can in principle be calculated, if the spatial power density profile of the laser beam is measured. The width of the resonance line for the transition shown in Fig. 18 (a) is dominated by the natural width $\Lambda = 1/(2\pi\tau) \approx 50$ MHz due to the short lifetime $\tau_{(36,33)} = 4$ ns of the final state (36,33). This can be reduced to less than 1 MHz by making a two-photon transition between two metastable states as shown in Fig. 18 (b). By using a laser pulse width of 30 ns or more, the associated Fourier width can be shortened to 5 MHz. The really limiting factor is the laser phase modulation or "chirp" which leads to a change of the laser frequency during the laser pulse itself. If the systematics of the pulsed $\overline{\mathrm{p}}$ beam, i.e. its intensity and position fluctuations – which are not known yet – are not considered, a resolution in the order of 50 MHz or a little less seems achievable with a simple injection-seeded pulse-amplified dye

Table 3: *Various factors that limit the current experimental accuracy to 0.5 ppm.*

Bandwidth of the pulsed laser	0.9 GHz
Collision-induced shift	~ 1 GHz
Collision-induced broadening	< 0.5 GHz
Doppler broadening	0.5 GHz

Table 4: *Additional factors that will limit future high-precision measurements.*

AC Stark effect	< 50 MHz
Natural width	$0.1 \sim 50$ MHz
Laser pulse width	10 – 50 MHz
Laser phase modulation	< 50 MHz
Systematics of pulsed beam	needs to be studied

laser. This corresponds to a relative precision of 70–80 ppb with respect to the 400–500 nm laser photons, and to an 7-fold improvement over the previously achieved accuracy.

In principle the 50 MHz limit can be overcome by performing a chirp-compensation using a more sophisticated laser system. Recently, the 1S–2S energy splitting of Muonium (μ^+e^-) has been measured at the Rutherford-Appleton Laboratory by two-photon spectroscopy using a chirp-compensated Alexandrite laser system with 10 MHz accuracy [14], which sets the standards for the achievable resolution in such an experiment. 10 MHz would in our case correspond to an accuracy of ~ 15 ppb.

While we are still in the process of selecting the best technical solution for the pulsed laser system needed, a proof-of-principle measurement of the two-photon method and the laser power needed can be made using our existing laser system by selecting a temperature where the Doppler broadening will significantly exceed the laser bandwidth of ~ 0.9 GHz. Such a measurement will be performed during next year

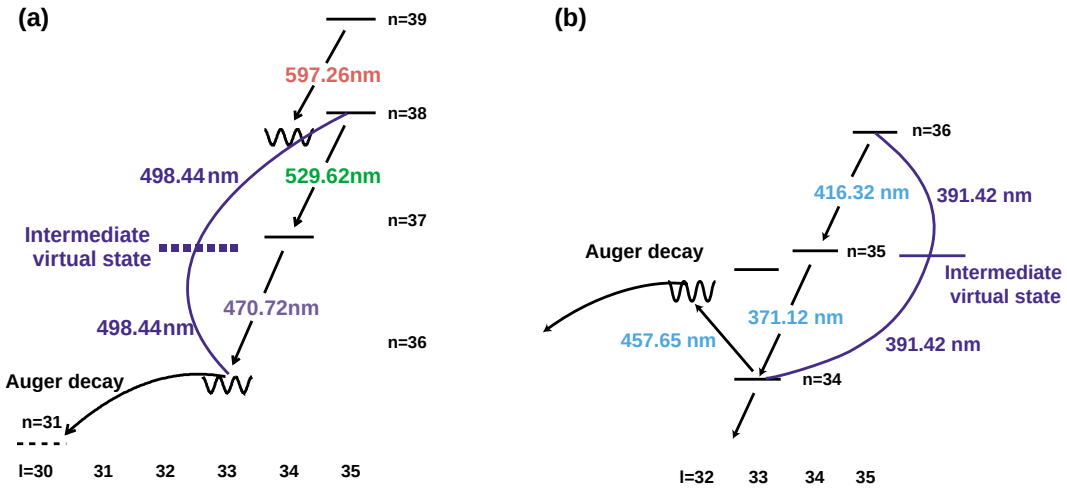

Figure 18: *Candidate transitions for higher-precision measurement of antiprotonic helium energy spacings. (a) The positions of the experimentally observed 597.26 nm, 470.72 nm, and 529.62 nm resonance lines are shown. The solid lines indicate radiation-dominated metastable states with lifetimes of 1–2 μs, the wavy lines Auger-dominated short-lived states. The proposed two-photon transition will be made between the states (38,35) and (36,33) using two counter-propagating laser beams with a wavelength of $\lambda = 498.44$ nm. The curved arrow indicates an Auger transition with minimum Δl to a state of ionized $\overline{\mathrm{p}}He^{2+}$ (dashed line), which is immediately destroyed due to Stark mixing induced by collisions with other helium atoms. The following prompt annihilation of the $\overline{\mathrm{p}}$ constitutes our experimental signature for a resonant transition. (b) 2-photon transition between metastable states (36,35) and (34,33) using two photons of $\lambda = 391.42$ nm. In this case another laser-induced transition is necessary to transfer the $\overline{\mathrm{p}}$ to a short-lived state (35,32). This transition can be made using a normal large-bandwidth laser as we already possess.*

at the AD.

An improvement of the experimental value to the described accuracy, in combination with the already achieved accuracy of the theory, would clearly improve the CPT constraints for the antiproton accordingly. Also, since the value of the proton mass is known only to 40 ppb [15] in units of eV/c^2 and therefore Rydberg, which is the "atomic unit" used in theoretical calculations for energies, an agreement of experiment and theory below 40 ppb would make it possible to extract a value for the antiproton mass which would be more precise than the proton mass! It should also be noted that in order to reach a sensitivity of 40 ppb for CPT test of the antiproton using 1S–2S spectroscopy of antihydrogen, a precision of 0.02 ppb is needed due to the indirect contribution of the $\overline{\mathrm{p}}$ mass through the reduced mass to the energy spectrum of the antihydrogen atom.

3.2.3 Studies of initial capture processes

To study the atomic formation process is one of the central parts of the ASACUSA programme. From the laser spectroscopy of antiprotonic helium atomcules, important information on the initial population of $\overline{\mathrm{p}}$ as a function of principal quantum number n and angular momentum quantum number l can be obtained. Fig. 19 shows the level diagram of $\overline{\mathrm{p}}^4$He. Experimentally observed laser transitions are denoted by bold arrows. From theses results, for the first time in the history of exotic atoms the commonly accepted hypothesis that negatively charges particles (here antiprotons) are initially captured around $n_0 \approx \sqrt{M^*/m}$, where M^* denotes the reduced mass of the atomcule and m the electron mass, could be proved. More detailed experimental data on initial population $P(n,l)$ come from the measurement of the trapping fraction f_{trap} and the time evolution of the resonance intensity of the observed transitions.

The theoretical distributions $P(n,l)$ have been calculated by a number of semi-classical models [16–18], all of which predict that 20–25 % of the stopped antiprotons form metastable atoms, with the higher-lying states with principal quantum number $n \geq 41$ containing the majority (cf. Fig. 20). The overall trapping fraction of $\overline{\mathrm{p}}$ in helium as measured at LEAR is ~ 3 %, nearly independent of the density and phase of the helium medium. Our laser spectroscopy studies also showed that the majority of $\overline{\mathrm{p}}$ occupy states of principal quantum number $n = 37-40$ with very little or no population in the region above $n \geq 41$, corresponding to the small fraction as indicated in Fig. 20. This discrepancy is large, but in general, it has not been established whether these theoretical models can be used to derive the accurate distribution of state populations of exotic atoms, since there exists little or no experimental data concerning the early stage of the formation process.

Direct comparison between the populations derived from these theoretical calculations, and the experimental results are difficult in any case, because while none of the theories take into account the effects of the thermalization process of $\overline{\mathrm{p}}\mathrm{He}^+$ atomcules, the existing experiments measure the state populations some 0.3 μs following formation in helium of typical densities of $\rho \sim 10^{20}$ cm^{-3}. At that time the atomcule has undergone many collisions with the surrounding helium atoms and thermalized to the target temperature. Some theoretical studies [18, 19] suggest that the observed discrepancy is due to the rapid quenching of the highly excited metastable states during the thermalization of the atomcule. Korenman [18] argues that, when the $\overline{\mathrm{p}}$ is captured into higher-lying excited states, the formed $\overline{\mathrm{p}}\mathrm{He}^+$ recoils with a correspondingly larger kinetic energy through the helium gas, which leads to a larger cross section for collisional quenching . His theory predicts, that all the states that lie above a certain critical threshold, characterized by the principal quantum number $n > 40 - -42$, have such a high recoil energy that they are quenched immediately after the atom has been formed.

By using the RFQ beam and helium gas at 6 K and 5 mbar corresponding to a density of $\rho \sim 6 \times 10^{18}$ cm^{-3}, three orders of magnitude lower than in previous measurements, a fraction of the theoretically predicted population become visible, leading to an increased trapping fraction and therefore also to a prolonged average lifetime of $\overline{\mathrm{p}}\mathrm{He}^+$ atomcules. At densities low enough that the mean time between collisions becomes comparable to the lifetime of the atomcule, also the thermalization process of $\overline{\mathrm{p}}\mathrm{He}^+$ can be studied.

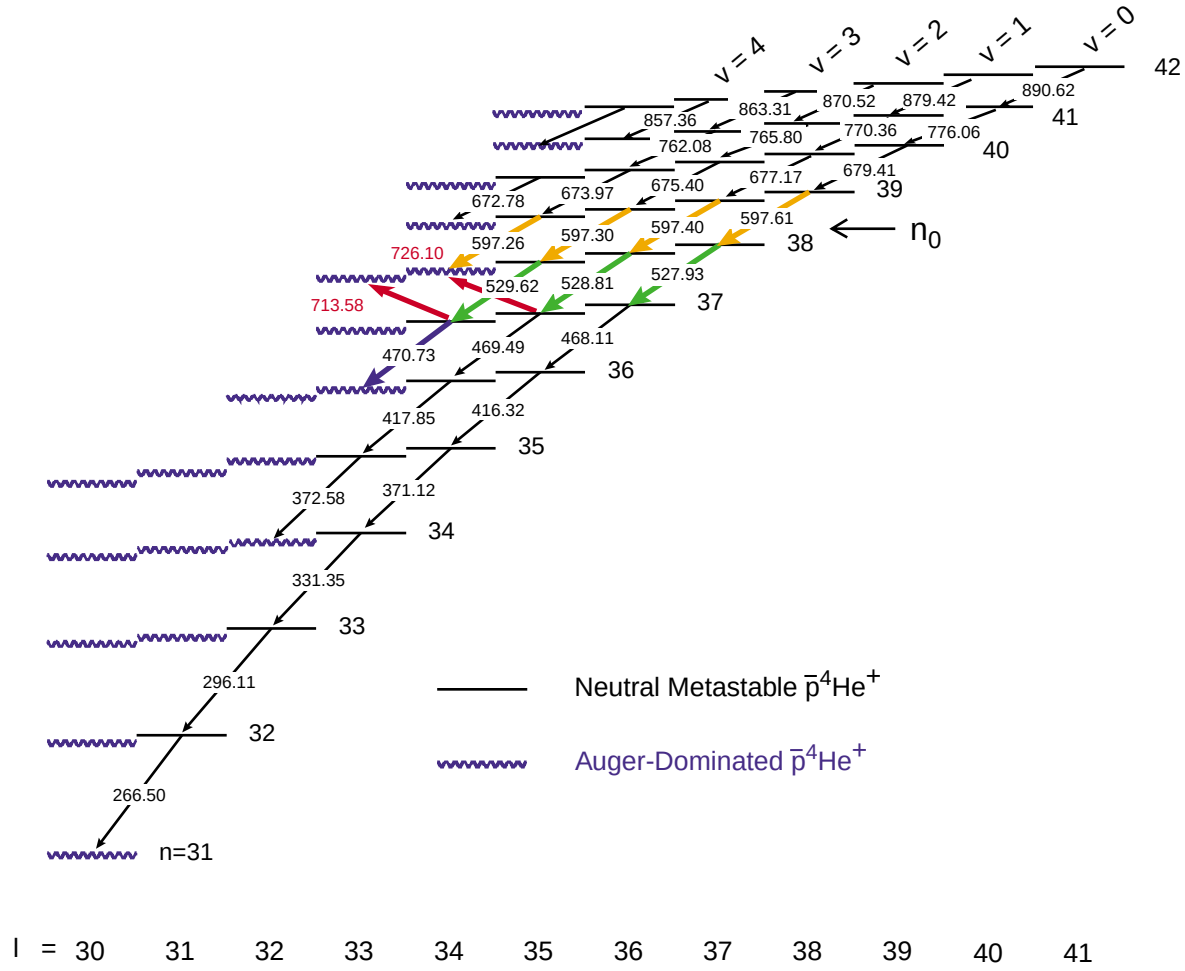

Figure 19: *Energy level diagram of antiprotonic helium and observed transitions (arrows). Metastable levels are denoted by straight lines, short-lived ones by wavy lines. The numbers correspond to the transition wavelength in nm.*

The populations of metastable states above $n > 40$ will be probed by the optical parametric oscillator extension to our dye laser which is already installed in the AD hall and which can cover the wavelength region up to 1100 nm and above.

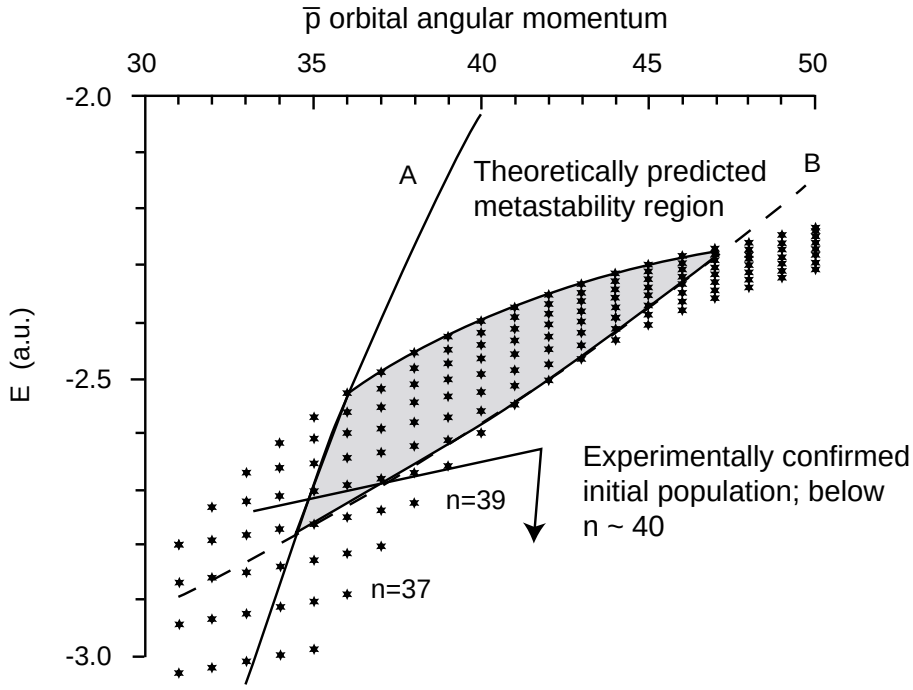

Figure 20: *Energy diagram of antiprotonic helium. The stars denote energy levels. According to a theoretical prediction of Korenman [18] the states between the lines A and B (grey region) are populated initially. Experimentally so far only population at* $n \leq 40$ *could be observed.*

4 Development of an ultra slow antiproton beam with the electron cooling technique

As had already been discussed in Section 4 of the previous ASACUSA Proposal submitted in 1997, there are a lot to be studied with monochromatic antiproton beams with energies in the keV to eV range, which had never been realized until now. Examples of research subjects are to study ionization processes of a few body system by slow negatively charged particles, to investigate antiprotonic atom formation processes under single collision conditions, etc. It is noted that various antiprotonic atoms are expected to keep their intrinsic metastability when they are in vacuum, which enables for the first time to make high precision spectroscopy of various antiprotonic atoms such as protonium ($\bar{p}p$), the simplest pure hadronic atom, $\bar{p}He^{++}$, etc.

4.1 Scheme of Ultra Slow Antiproton Production

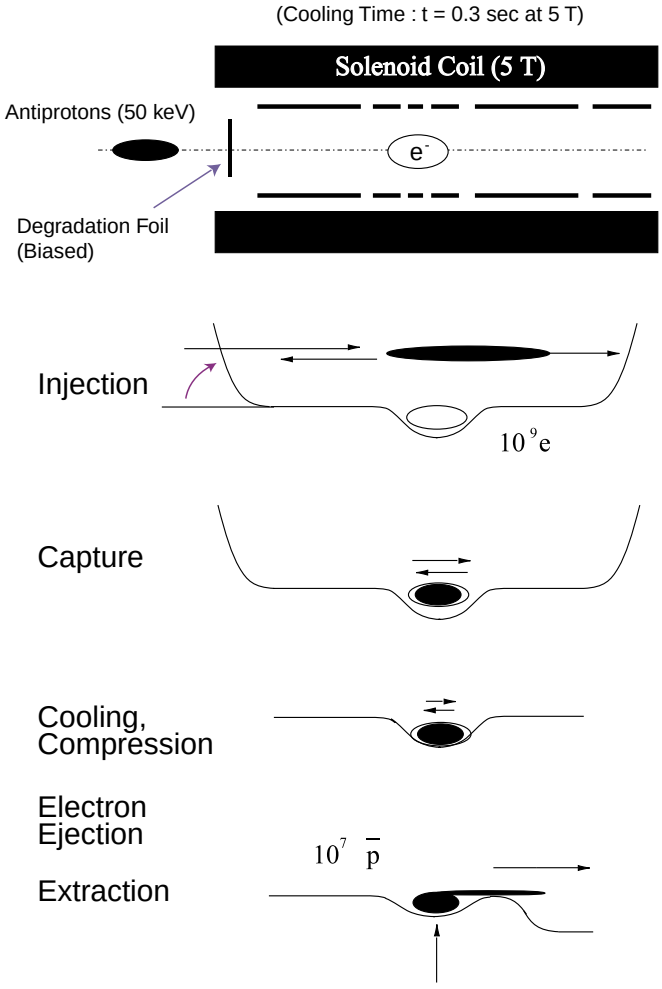

Figure 21: *A schematic procedure to trap, cool, compress, and extract antiprotons*

A schematic diagram of the antiproton cooling procedure is given in Fig.21 [20]. In order to capture antiprotons of several tens keV from the RFQ with rather low trapping potential, a thin degrader foil is inserted between the RFQ and the trap. The foil can be positively biased, which effectively reduces the energy

straggling of the degraded beam and eventually increases the trapping efficiency. The antiprotons passing through the degrader foil are reflected by the negatively biased Catching Electrode 2 of the ASACUSA Trap (see Fig.23. Before the reflected antiprotons return to the left end of the trap, the Catching Electrode 1 is biased from 0 to < -10kV, which results in trapping antiprotons. In the trap, electrons are pre-loaded, which are cooled via synchrotron radiation with an empirically determined time constant $t_{rad} \sim 0.3$sec at 5T. The cooled electrons then sympathetically cool the trapped antiprotons via the Coulomb interaction within 1-10 sec in the present case. Once the antiprotons are cooled, a rotating electric field is applied to radially compress the antiproton and electron plasma. Antiprotons thus cooled and sharpened are eventually extracted from the trap. A DC extraction is performed by slowly ramping up the bottom of the trap potential. A similar method had been shown to be very stable and reliable for extraction of positrons with an energy width of $\sim$18 meV [21]. A pulsed extraction will also be possible by applying a pulse train on the trapping electrode.

4.2 Superconducting Solenoid and the ASACUSA Trap

Figure 22 shows a drawing of the superconducting solenoid, which is designed so that

1. it delivers the magnetic field of 5T
2. the bore with its inner diameter of 165mm can be cooled as low as 6K and is bakable keeping the superconducting magnet at liquid helium temperature
3. the bore is independently movable to align the trap axis to the symmetry axis of the magnetic field, which is essential for a successful extraction of ultra slow antiprotons
4. the magnetic field is scannable at 5T/90sec, which allows to vary the field strength depending on the operational stage, i.e., injection, cooling, or extraction.

The whole procedures to prepare ultra slow $\bar{p}$, i.e., trapping, cooling, and extraction are under study with p and H^-.

A drawing of the ASACUSA trap is shown in Fig. 23, which consists of 14 cylindrical electrodes of 40 mm in inner diameter and total length of $\sim$500 mm, all of which are mounted on a stage machined with 20 μm precision. The trap has been designed to have a long harmonic potential region and to store as many as $\sim 5 \times 10^6 \bar{p}$s and about 100 times more electrons in a prolate spheroid with a radius $\sim$ 1 mm and its axial length $\sim$ 50 mm with a rather low trapping potential. The advantages of the ASACUSA trap are [22]

1. the lifetimes of particles are much longer than those in a square well trap
2. the axial length of the plasma automatically increases when the plasma is compressed radially, which helps to reduce the plasma heat up
3. the axial motion of the plasma can be used for diagnostics.

As low energy charged particles tend to follow the field line, it is essential to locate the position of the particles in the trap as close to the magnetic field axis as possible to realize the extraction of high quality antiprotons beams. The multi-ring structure is exploited to generate the harmonic potential [23] [24]. A rotating electric field exerts a torque on the plasma so that the plasma is squeezed radially [25]. Such a rotating field also suppresses radial diffusion of charged particles across the magnetic field line which are induced by internal collisions. In order to apply the rotating field, one of the cylindrical electrode in the harmonic part of the trap is segmented into four (see Fig. 23).

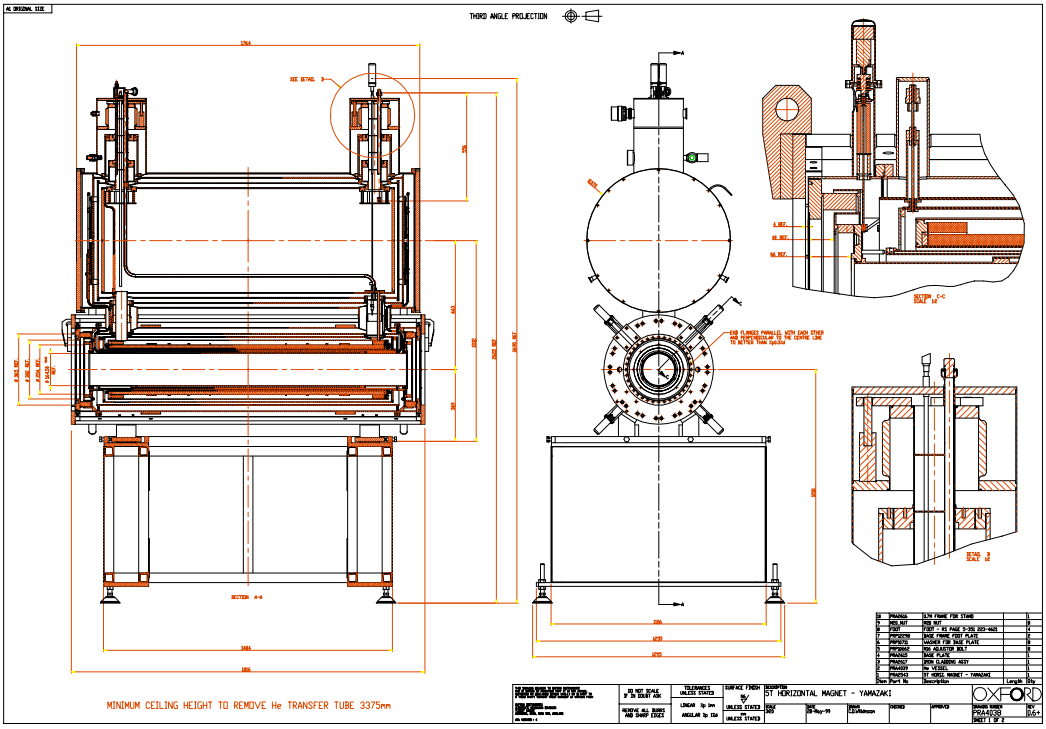

Figure 22: *A drawing of the 5T superconducting solenoid*

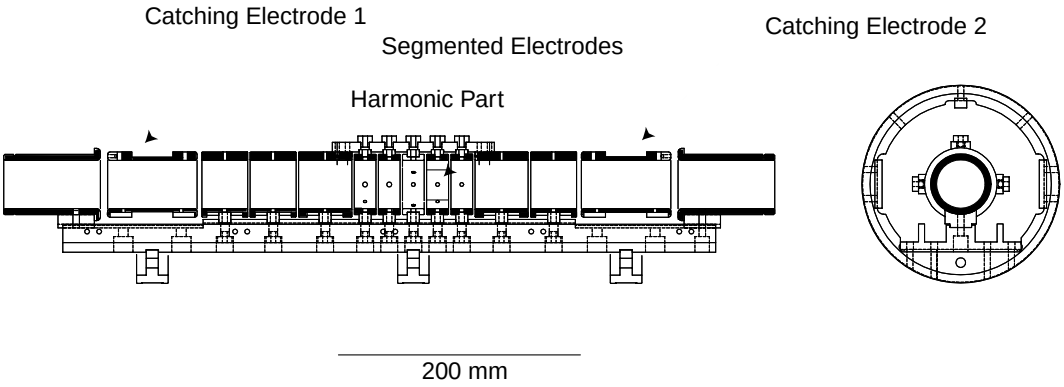

Figure 23: *A drawing of the ASACUSA trap*

It is noted that the trapping efficiency of the present setup combined with the RFQ is expected to be about two orders of magnitudes higher than that obtained by a conventional trapping scheme, *i.e.* , the combination of a degrader foil and an electro-magnetic trap.

Figure 24 shows the radial distribution of electrons stored in the ASACUSA trap for 10sec (a) with and (b) without the rotating field. It is seen that the rotating field compressed the electron plasma substantially.

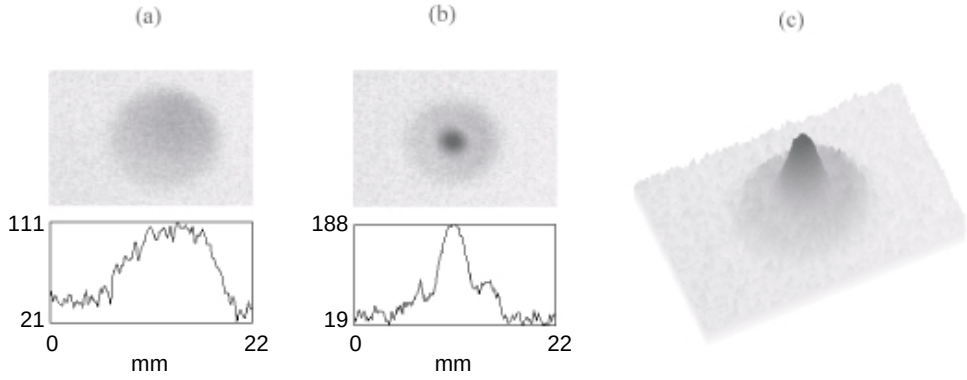

Figure 24: *The radial distribution of electrons stored for 10sec in the trap (a) without, (b) with the rotating electric field. Figure (c) shows the 3D image of (b).*

4.3 Extraction of Antiproton Beam

Cooled antiprotons are extracted from the trap, and transported to the target chamber. The extraction beamline is designed to fulfill the following requirements, *i.e.* ,

1. An electrostatic lens system has to be prepared so that antiprotons passing a region of a strongly divergent magnetic field can be transported without suffering large divergence and without suffering loss of antiprotons for a wide energy range from 10 to 1500 eV.

2. The beamline has to function also as a differential pumping system so that the pressure difference of more than 5 orders of magnitudes (from 10^{-6} Torr to 10^{-11} Torr) is maintained

The upper half of Fig. 25 exhibits the arrangement of transport elements to realize the above requirements. The cold antiprotons inside the trap located in the center of the bore tube move slowly to the right. In the cylindrical electrode denoted as EXTRACTOR, the antiprotons are transported with their kinetic energy around 250 eV. Two sets of x-y deflectors are placed in the EXTRACTOR, which enable fine adjustment of the beam position as well as its direction. Downstream of the EXTRACTOR, two Einzel lenses, LENS 1 and LENS 2, are prepared, which are designed to be operated under ”acceleration mode”. In this case, the antiprotons are sharply focused at the center of each Einzel lens. The trajectories are calculated assuming that antiprotons having kinetic energies less than 1 eV are confined in a cylinder of 1 mm in radius and 50 mm in length. The lower half of Fig.25 presents the envelope (r against z) of antiproton trajectories. The LENS 3, a decel/accel lens, is prepared to deliver well-collimated antiprotons of 10-1500 eV. at the target position. It is seen that the antiproton beam is focused at z=3.125m from the center of the trap with a spot diameter of around 7 mm.

The sharp focus realized at the center of each lens allows to place a small adjustable aperture of $\sim$3mm in diameter, which enables to make a very efficient differential pumping without loss of antiprotons.

Further, three 40mm gaps are prepared between the EXTRACTOR and the LENS 1, the LENS 1 and the LENS 2, and the LENS 2 and the LENS 3 to place gate valves.

Two different types of beam profile monitors (BPM) has been developed. The first system is a position sensitive detector consisting of a microchannel plate and a delay line, which is remotely retractable from the beam axis to path antiprotons further downstream. This MCP-BPM is sensitive enough to detect single antiproton, and monitors the beam profile during DC extraction. The second system is a multi wire chamber, which offers nondestructive beam profile monitoring when a pulsed antiproton beam is extracted. An extraction scheme to produce microbunches of pulse widths 500-1000 ns with 10 Hz repetition rate, which could be accelerated up to 50 keV are under preparation.

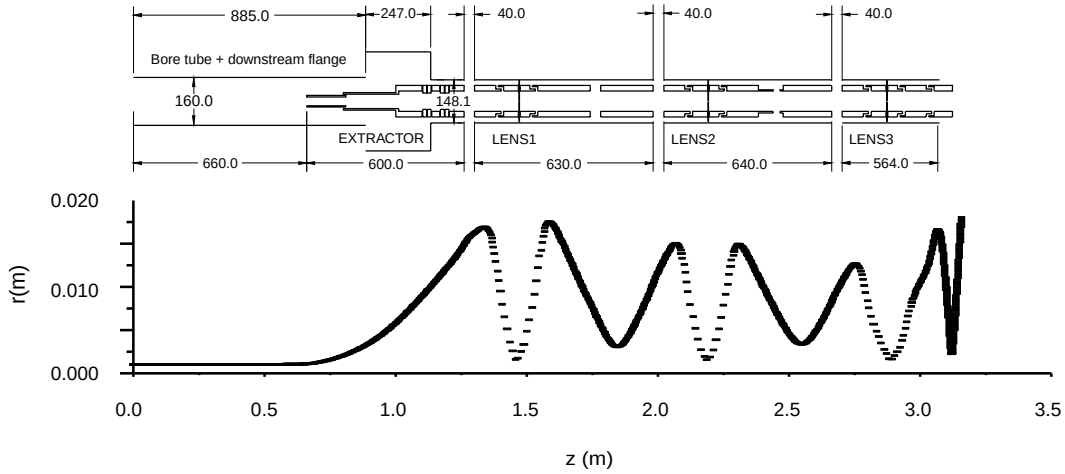

Figure 25: *The configuration of the beam transport elements for ultra slow antiproton beams (upper). Calculated beam envelope of antiprotons starting at 1 eV inside the trap with a radius of 1 mm. The final beam diameter at z=3.125 m inside the experimental chamber is about 7 mm. The kinetic energy of the beam at the target position is 10 eV (lower).*

All the steps necessary to provide a cold monoenergetic antiproton beam of high quality will be tested using H^- as a substitute for antiprotons.

References

[1] T. Azuma et al., (ASACUSA Collaboration), Proposal CERN/SPSC 97-19, CERN/SPSC P-307 (1997).

[2] H. A. Torii et al., Phys. Rev. A 59 (1999) 223.

[3] V. I. Korobov and D. D. Bakalov, Phys. Rev. Lett. 79 (1997) 3379.

[4] N. Elander and E. Yarevsky, Phys. Rev. A 56 (1997) 1855, Errata Phys. Rev. A **57**, 2256 (1998).

[5] Y. Kino, M. Kamimura, and H. Kudo, Nucl. Phys. A 631 (1998) 649c.

[6] V. I. Korobov, in *Proceedings of the Asia-Pacific Few Body Conference (APFB99)*, Kashiwa, 1999, Few Body Systems Suppl., in press.

[7] V. I. Korobov, private communication, 1999.

[8] W. Barkas, W. Birnbaum, and F. M. Smith, Phys. Rev. 101 (1956) 778.

[9] S. P. Møller et al., Phys. Rev. A 56 (1997) 2930.

[10] We wish to thank K. Iversen, ISA, Aarhus, for producing the construction drawings and for making everything fit.

[11] A. Adamo et al., Phys. Rev. A 47 (1993) 4517.

[12] M. Agnello et al., Phys. Rev. Letters 74 (1995) 371.

[13] C. Caso et al., The European Physical Journal C 3 (1998) 1.

[14] K. Jungmann, private communication, 1999.

[15] P. J. Mohr and B. N. Taylor, Reviews of Modern Physics 72 (2000).

[16] N. Morita, K. Ohtsuki, and T. Yamazaki, Nucl. Instrum. Methods Phys. Res., Sect. A 330 (1993) 439.

[17] W. A. Beck, L. Wilets, and M. A. Alberg, Phys. Rev. A 48 (1993) 2779.

[18] G. Ya. Korenman, Hyperfine Interact. 103 (1996) 341.

[19] M. Hori, PhD thesis, University of Tokyo, 2000.

[20] Y. Yamazaki, Nucl.Instrum.Methods B154 (1999) 174.

[21] S. Gilbert, R. Greaves, and C. Surko, Phys.Rev.Lett. 84 (1999) 5032.

[22] T. Ichioka et al., Proceedings of the International Workshop on Nonneutral Plasmas (1999).

[23] H. Higaki and A. Mohri, J.J.Appl.Phys. 36 (1997) 5300.

[24] A. Mohri et al., J.J.Appl.Phys. 37 (1998) 664.

[25] F. Anderegg, E. Hollmann, and C. Driscoll, Phys.Rev.Lett. 78 (1998) 4875.

[26] P. Dahl, *Introduction to electron and ion optics*, Academic Press, 1973.

[27] H. Bethe, Ann. Phys. 5 (1930) 325.

[28] E. Harting and F.H.Read, *Electrostatic lenses*, Elsevier Scientific, 1976.

[29] N. Bohr, Phil. Mag. (6) 30 (1915) 581.

[30] J. Lindhard and M. Scharff, 27, No. 15 (1953).

[31] A. Sørensen, Nucl. Instr. Meth. B 48 (1990) 10.

[32] P. Sigmund and K. Winterbon, Nucl. Instr. Meth. 119 (1974) 541.

[33] A. Belkacem and P. Sigmund, Nucl. Instr. Meth. B 48 (1990) 29.

[34] H. Klette, CERN, private communication.

A Appendix – ElectroStatic Analyzer (ESA) design detail[2]

The first draft for the construction of an electrostatic analyzer (ESA) to investigate the stopping power of antiprotons in thin foils and gases - as found in the first ASACUSA proposal[1] – consisted of two electrostatic deflectors between which the target was placed. The present study aims to define the necessary parameters for the actual realization of this apparatus, while at the same time providing more accurate numbers on *e.g.* transmission efficiency, resolution and lower limit of energy.

A.1 ESA electrodes

We choose spherical electrostatic analyzers since they provide stigmatic focusing, *i.e.* equal focusing in the horizontal and vertical planes (for a discussion of electrostatic analyzers, see eg. ref. [26]). Therefore we can obtain a small beam in both transverse directions at the position of the gas cell.

A.2 Dispersion

In order to be able to select particles of different energy and momentum, it is necessary to have a large dispersion and a focal point at the position of the gas cell. The dispersion is given as $D = 2R(1 - \cos(\varphi))$ for a spherical ESA, where $\Delta r = D\Delta p/p$ is the deviation from the equilibrium orbit at the output where the particle has been deflected through an angle φ. A requirement $\Delta p/p = 0.05$ (The intrinsic spread of the RFQ beam is $\Delta T = 9$ keV) and a minimum resolution of $\Delta r > 10$ mm which with $\Delta r = 2R\Delta p/p$, $L = \varphi R$ for maximum dispersion, $\varphi = 90^\circ$, leads to $L > \Delta r \cdot \pi p/4\Delta p = 157$ mm or $R > 100$ mm.

A.3 Length of electrodes, radius of curvature

The centripetal force necessary for a curved trajectory equals $F = eE_0 = mv^2/R$, where e is the magnitude of the electron charge, E_0 the electric field in the center of the gap, m the mass of the antiproton, v its speed and R the radius of curvature. The kinetic energy is $\epsilon = \frac{1}{2}mv^2$ and the electric field for a spherical analyzer is $E(r) = E_0(r/R)^{-2} \approx E_0(1 - 2x/R)$ where the last approximation is for a gap d much smaller than R and $r = x + R$. To second order in d/R this leads to the field $E_0 = \Delta V/d \cdot (1 - d^2/4R^2) \approx (V_1 - V_2)/(r_1 - r_2)$where V_i are the potentials, r_i the radii of the analyzers and d the gap distance. Thus we get $\epsilon = \frac{1}{4}e(V_1 - V_2) \cdot (r_1 + r_2)/(r_1 - r_2)$ which by $R = (r_1 + r_2)/2$ and $d = (r_1 - r_2)$ gives $\Delta V/d = 2\epsilon/eR$. This field strength is limited due to the risk of sparks by $E_{\max} = \Delta V/d|_{\max} < 1$kV/mm and since $\epsilon < \epsilon_{\max} = 100$keV we get a minimum radius of curvature $R > R_0 = 2\epsilon_{max}/(eE_{\max}) = 200$mm. With the restriction on the electrode length $L > 157$ mm we get a constraint on the deflection angle $\varphi > 45^\circ$, *i.e.* no contradiction with the above. We choose a deflection angle of 90° (as seen above this maximizes dispersion and makes sure that the initial drift is not excessive while making place for the gas cell) and a length 392.7 mm, *i.e.* $R = 250$mm, which leaves only a small margin against electrical break-down at the maximum energy, but surely enough margin at 50 keV. This radius of curvature coincides with that supplied for standard beam line tubes and will thus secure minimum cost.

A.4 Gap distance

Simulations show that the maximum beam radius (2σ, 95% of all particles) in the ESA is of the order 9 mm which means that half the gap distance must exceed this with some safety margin to account for mis-steered beam etc. (still, 68% is contained within 4.5 mm). Therefore we choose $d = 20$ mm and get

[2]Excerpt from a report CERN PS/CA Note 99-23, H. Knudsen, U. Mikkelsen, S.P. Møller, R. Thompson and E. Uggerhøj, unpublished

$\Delta V_{\max} = d \cdot E_{\max} = 2\epsilon_{\max} d/eR$ to be $\Delta V_{\max}[\mathrm{kV}] = d[\mathrm{mm}]/1.25$ which means maximum 8 kV on each electrode.

The gap distance is also limited by $d \ll L$ and $d \ll h$ where h is the height of the electrodes to avoid significant edge focusing effects. Thus the choice of d sets a limit on h to be at least 50 mm. At the same time, the electrodes should fit into a standard beam tube with an inner diameter of 150 mm with a spacing of at least 20 mm to each side. With these restrictions, we choose h to be 60 mm to make room for the mounting and screening plates to make the field as homogenous as possible between the ESAs.

A.5 Gas cell

First, the beam size must not vary excessively within the volume. This variation is given (assuming a focus at the center) as $r_e/r_c \approx (1 + s^2/b^2)^{1/2}$ where r_e/r_c is the ratio of beam radii at the center and the edge of the gas cell a distance s away. $\beta \approx 5$cm is the Twiss parameter which determines the beam size from $(\epsilon_e \beta)^{1/2}$ where $\epsilon_e \approx 100\mathrm{mm} \cdot \mathrm{mrad}$ is the emittance. From $s = L_g/2$, where L_g being the length of the gas cell, the calculated value $r_c \approx 1$mm (again 95% of all particles) and the constraint $r_e < 1.5$mm given by the diameter of the entry- and exit-windows, we get $L_g < 2\beta((r_e/r_c)^2 - 1)^{1/2} = 112$mm.

The length of the gas cell must also be chosen such that energy loss in a gas of reasonable pressure is comparable to the loss in the two windows confining the gas. Windows for the gas cell can be made of aluminum or carbon, $\phi 3$mm, $\Delta x = 500$Å thick. The energy loss is essentially proportional to the density of electrons [27]: $-dE/dx \propto NZ$ and since the pressure $p = nR_gT/V$ and the atomic density in Å^{-3}, $N = n/V = 0.6022 \cdot \rho/M$, with M the atomic mass in u and the density ρ in g/cm^3 we get with the gas constant $R_g = 8.314$J/(mol·K)$N_0 = 2.45 \cdot 10^{-5}$ atoms/Å^{-3} at $p = 1$atm. To limit the extent of gases we set $Z > 5$ and a reasonable pressure $p = 1/100$atm. (The number of collisions is $n_{\mathrm{coll}} = N\sigma\Delta x$ where $\sigma \approx 1$ Å^2 is the excitation cross section, so the pressure must be $p \gg 1\mathrm{atm.}/(N_0\sigma\Delta x) > 3.6 \cdot 10^{-5}$ atm. to fulfill $n_{\mathrm{coll}} \gg 1$ for the stopping power measurement to make sense). This leads to a restriction on the gas cell length of $L_g > 2\Delta x(NZ)_{\mathrm{Al}}/(NZ)_{\mathrm{gas}} = 3.2 \cdot 10^6 \cdot 1000$ Å$/Z = 64$mm. We choose $L_g = 100$ mm.

The gas cell can be floated at a maximum potential of 10 kV to enease beam transport at low impact energies.

A.6 Length of drifts

Clearly, the drift between the ESAs must exceed L_g and leave room for diagnostics and apertures. Once the length of this drift region is fixed, the initial and final drifts are found from $L_a = L_c = 2R^2/L_b$ (with $\varphi = 90°$) which ensures a focus in the center of the gas cell. One must therefore find a compromise between a small $L_a = L_c$ or a small L_b. To get a fairly small beam size through the ESAs we choose $L_a = L_c = 250$mm and $L_b = 500$mm.

A.7 Simulations

Two kinds of simulations were performed. A simulation by use of SIMION was done to study influence of edge effects, apertures and other realistic parameters, see figure 28. For instance, it turns out that the position of the vertical focus at the gas cell is influenced by the height of the electrodes, h. The second calculation was done by use of MathCad to study the behaviour of beam size, dispersion, divergence and stability as a function of the ESA angle, φ, the drift lengths, L_a, L_b, L_c and the electrode length, L. Transformation of the initial Twiss parameters was done by matrix multiplication through the entire electrostatic lattice. Consistency with the behaviour predicted by SIMION was confirmed and the free variables were optimized to yield a large effect of dispersion at the output and in the gas cell while keeping the beam size small in both locations. At the same time, the stability of the solutions against errors of construction, *e.g.* angle or electrode length errors could be checked. The figures 26–28 show some examples.

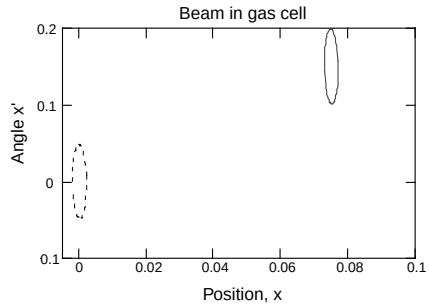

Figure 26: *Phase-space of the beam at the position of the gas cell. The full-drawn ellipse represents the beam including dispersion and the dashed excludes dispersion. The values used are an energy of 60 keV and a spread of 9 keV.*

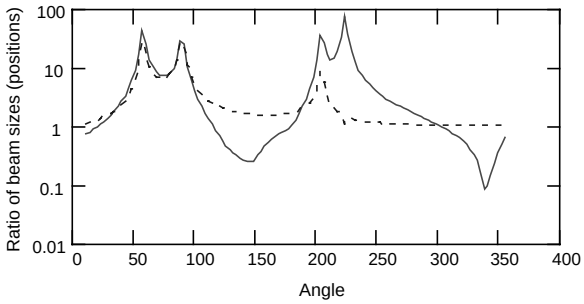

Figure 27: *Ratio of beam size+position with and without dispersion as a function of angle for* $L = 0.3927$*m. The dashed curve is the effect of dispersion through the last ESA only, whereas the full drawn shows the effect with dispersion in both ESAs.*

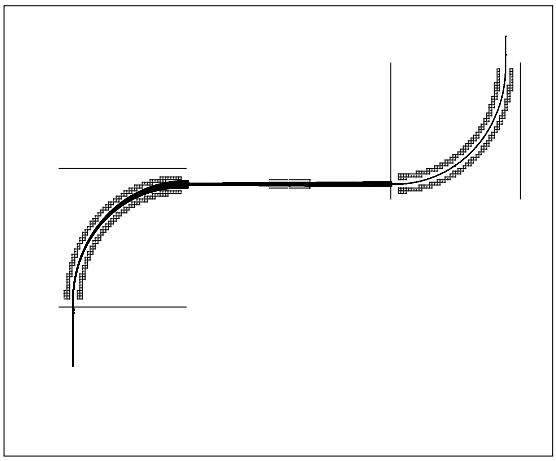

Figure 28: *SIMION simulation of the trajectory through the setup for different energies. The selections imposed by the apertures at the entry and exit of the ESAs are clearly seen.*

A.8 Beam steering

Parallel plate deflectors can be inserted upstream the first ESA and up/downstream the gas cell to correct for wrong steering. The deflection angle, α, of a particle with energy ϵ through a parallel plate deflector of length, L_p, with a field $\Delta V_p/d_p$ is given as $\alpha \approx e\Delta V_p L_p/2\epsilon d_p$. Thus, even for the 100 keV beam a short assembly, say $L_p = d_p = 20$mm, would suffice. For additional focusing, an Einzel lens could be inserted on the entry side of the ESAs. The focal length, f, of an Einzel lens consisting of 3 cylindrical electrodes of diameter D and length $0.9D$ separated by $0.1D$ is given as $f = 0.91 \cdot D\epsilon/V$ where V is the potential of the outer electrodes with respect to the central one which is kept at ground[28]. Thus, a lens with $D = 2$cm would yield a minimum focal length of 18 cm at 10 keV with the maximum voltage, $V = 2$kV. As it turns out, in order to make a compact apparatus, the gas cell cannot be positioned exactly in the center between the two outer spherical deflectors. The Einzel lens is thus essential to move the focal point of the beam such that the counting rate can be maximized.

A.9 Particle detection and diagnostics

To be able to get the beam through the whole setup, we need diagnostics along the way. We choose a retractable phosphorized channelplate screen with a camera in front of the gas cell and at the exit of the last ESA. The camera with a frame-grabber for further data-analysis enables single particle detection with a resolution of about 0.2 mm.

Furthermore, as the number of particles which will appear at the end detector may be quite small for the low energy measurements, particle counting can be enabled by conversion of the analog signal in an ADC while the beam spot is visible by use of the camera.

A.10 Estimated count rates, lower limit of energy

The lower limit of energy at which it makes sense to derive a stopping power is essentially determined by the energy loss straggling in the Al (or C) windows. Taking a total of $\Delta x = 1000$Å for the windows we get from Bohr's formula[29], $\Omega^2 = 4\pi N Z_2 e^4 \Delta x$ a straggling of $\Omega_{\mathrm{Al}} = 1.4$keV and $\Omega_{\mathrm{C}} = 1.3$keV (the so-called LS modification to the straggling formula[30] would lead to only $\Omega_{\mathrm{Al}} = 0.4$keV and $\Omega_{\mathrm{C}} = 0.4$keV) at 4 keV. The energy loss in Al from an electron gas calculation[31] which includes the Barkas effect, $\Delta E = 0.9C_1 \times 4Z_1 v e^2 \Delta x/(3\pi\alpha c a_0^2)$ equals 2.4 keV with $C_1 = 0.31$ for Al and about the same for C, also for antiprotons at 4 keV.

Furthermore, the increase of the emittance following the scattering in the foil is given as $\Delta\epsilon = \pi\beta\theta^2/2$ where θ is the RMS angle from multiple scattering found from $\theta = \pi a N \Delta x Z_1 Z_2 e^2/(Mv^2)$ and $a = 0.8853 a_0 Z_2^{-1/3}$ is the Thomas-Fermi screening distance[32]. This will enlarge the beam at the output such that starting with 10^7 particles and accounting for RFQ deceleration efficiency, emittance increase, straggling and apertures we get around 50 particles through the whole setup into a detector of 10 mm width. This detector width yields an energy resolution of 0.3 keV and the 3 mm aperture at the gas cell selects the initial beam to a width of 0.4 keV. It thus seems reasonable to state that around 4 keV is the lower limit for a measurement of the energy loss in a closed gas cell (the gas in the gas cell has not even been taken into account) for the proposed setup. However, with a few mm aperture at the output, it should be possible also to measure the energy straggling down to an energy of 4 keV – this may be of interest for protons as well as for antiprotons.

In the case of a continuation of the measurement by the use of foils, the constraint $\Delta E/E < 1$ calls for thin targets, $E > 2.9 C_1^2 Z_1^2 \Delta x^2 e^4/(M\pi^2\alpha^2 c^2 a_0^4) = 1.5 \cdot 10^{-3} \cdot \Delta x^2$eV/Å^2 for Al. This may be necessary since the stopping power in foils may not be described in the same way as that of gases at low energy even though calculations indicate that the dependence of the stopping power per target electron on the density of electrons is very weak over several orders of magnitude[33]. Foils of 500 Å Si, Al or C can be prepared

where the energy loss amounts to about 0.5 keV which would bring the realistic minimum of energies down to a few keV. Such foils with a diameter of 3 mm have recently been tested and shown to withstand a pressure of up to about 40 mbar, see figure 29. From this figure it is also seen that not all the displayed carbon foils are of the same quality in terms of homogeneity and the Al foils investigated (not shown) have a leakage rate of about a factor 3 higher for the same thickness.

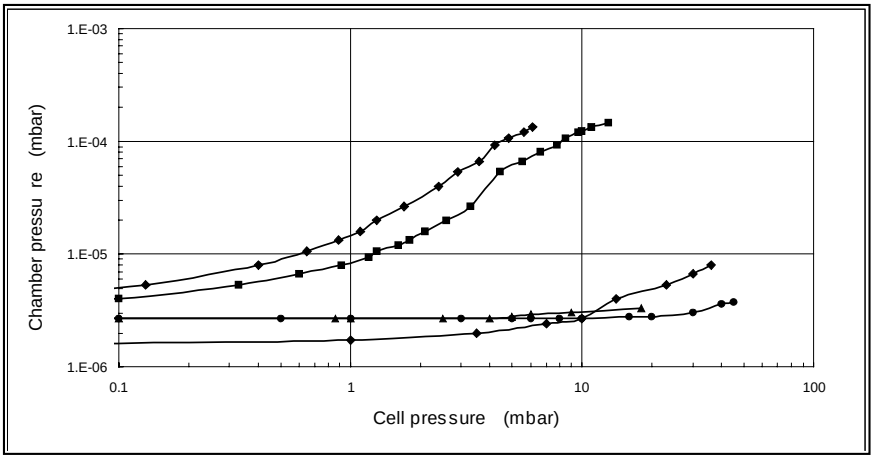

Figure 29: *Chamber pressure as a function of pressure in the gas cell. The endpoint of each curve indicates the pressure at which the window ruptures.*

One way to get to even lower energies is by using a differentially pumped gas cell, *i.e.* simply the same setup except for the entry- and exit-windows. One can then calibrate the average pressure in the open gas cell by measuring stopping powers in a region overlapping in energy with those of the complete gas cell. This may bring the lower limit of energies down to the eV region to verify earlier indirect evidence of the nuclear stopping power[12]. The conductivity of a ϕ 3 mm cylinder of length 10 mm is sufficiently low and furthermore two discs with ϕ 10 mm holes are introduced to isolate the region of the gas cell to the turbo pump. Since the vacuum requirements for the RFQ is 10^{-6} or better, a turbo pump is needed at the gas cell[34] as well as a pump supplied by CERN at the exit of the RFQ.

A.11 Calibration - cross check

We propose to calibrate the setup in terms of energy by a measurement of the time-of-flight of the ions. This can be done with respect to the RF cycle of the RFQ and the AD and by measuring the arrival time for the undecelerated 5.31 MeV antiproton beam from the RFQ. For this reason, and to dispose of the undecelerated beam without generating too many pions that can trigger downstream detectors, a hole in the first spherical analyzer covered with a fine mesh will be made. The dump will be constructed from a 2 mm thick tantalum foil placed at the end of a steel cylinder. This has the advantage that the main component of induced activity (which may be significant after tests with protons) is low energy electrons which will not penetrate the steel.

As an alternative to the undecelerated antiprotons, one may use a source of electrons with energy similar to that obtained for the antiprotons from the RFQ. Initial testing with protons in Aarhus will give a rough calibration of the setup with beam momentum as a function of ESA voltages.

In terms of pressure in the gas cell a precise measurement should not be too difficult *e.g.* by means of a baratron, since it is a confined volume where tests of the windows show very limited leakage through the windows for pressures in the range up to 1/100 atm.